

Proton distribution visualization in perovskite nickelate devices utilizing nanofocused X-rays

Ivan A. Zaluzhnyy,^{1,*} Peter O. Sprau,^{1,†} Richard Tran,² Qi Wang,³
 Hai-Tian Zhang,^{3,4} Zhen Zhang,³ Tae Joon Park,³ Nelson Hua,¹ Boyan
 Stoychev,¹ Mathew J. Cherukara,⁵ Martin V. Holt,⁵ Evgeny Nazaretski,⁶
 Xiaojing Huang,⁶ Hanfei Yan,⁶ Ajith Pattammattel,⁶ Yong S. Chu,⁶
 Shyue Ping Ong,² Shriram Ramanathan,³ Oleg G. Shpyrko,^{1,*} and Alex Frano^{1,*}

¹*Department of Physics, University of California San Diego, La Jolla, CA 92093, USA*

²*Department of NanoEngineering, University of
California San Diego, La Jolla, CA 92093, USA*

³*School of Materials Engineering, Purdue University, West Lafayette, IN 47907, USA*

⁴*Lillian Gilbreth Fellowship Program, College of Engineering,
Purdue University, West Lafayette, IN 47907, USA*

⁵*Center for nanoscale materials, Argonne National Laboratory, Argonne, IL 60439, USA*

⁶*National Synchrotron Light Source II,
Brookhaven National Laboratory, Upton, NY 11973, USA*

Abstract

We use a 30-nm x-ray beam to study the spatially resolved properties of a SmNiO₃-based nanodevice that is doped with protons. The x-ray absorption spectra supported by density-functional theory (DFT) simulations show partial reduction of nickel valence in the region with high proton concentration, which leads to the insulating behavior. Concurrently, x-ray diffraction reveals only a small lattice distortion in the doped regions. Together, our results directly show that the knob which proton doping modifies is the electronic valency, and not the crystal lattice. The studies are relevant to on-going efforts to disentangle structural and electronic effects across metal-insulator phase transitions in correlated oxides.

* Corresponding authors: izaraluzhnyy@physics.ucsd.edu, oshpyrko@physics.ucsd.edu, afrano@ucsd.edu

† These two authors contributed equally: Ivan A. Zaluzhnyy and Peter O. Sprau

I. INTRODUCTION

Among possible replacements for density-limited silicon transistors on integrated circuits are quantum materials, such as transition metal oxides. These are promising because their electronic properties can be tuned efficiently and reversibly. For example, they have recently gained attention as a platform for devices that could enable neuromorphic computing, which offers a new level of computational efficiency by creating artificial systems that can emulate the operation of animal brains [1, 2]. This requires development of hardware elements whose electrical resistance changes under external stimuli (e.g., voltage or light pulse), emulating synaptic memory links between neurons [3, 4]. Prospective materials for these new electrical elements must a) be electrically switched by a small external stimulus, b) have a wide range of electrical resistance, c) increase or decrease resistance with stimuli, and d) operate at room temperature.

Not many materials exist that can satisfy all these requirements. Among them, rare-earth nickelate SmNiO_3 (SNO) doped with protons H^+ (H-SNO) is an extremely promising candidate, especially due to controllability of the switching process [3, 5–7]. Moreover, the design of the nanodevice with synaptic functionality is as simple as a proton-doped SNO film between two metallic electrodes [8]. The synaptic behavior of such a memory device fundamentally relies on the motion and redistribution of protons influenced by electric field pulses. This raises two questions: a) how does proton doping change the structure and properties of SNO at the nanoscale, b) how protons are distributed in the SNO film? Understanding these phenomena is important from a fundamental point of view.

X-rays have been traditionally used to determine the properties of pristine nickelate heterostructures [9, 10], but in small synaptic devices, the key challenge is to determine how the spatial distribution of protons affects the electrical properties of SNO. Additionally, x-rays do not directly detect light ions easily, but instead they are a perfect tool to study the influence of doping on the electronic and crystal structure of SNO. To overcome these challenges, we uniquely probed the device with nanofocused x-ray beam to pinpoint the origins of resistive switching trends in SNO and disentangle, whether it is a structural or electronic change that drives the modulation in resistance. By studying the x-ray fluorescence spectra near the Ni K-edge supported by *ab initio* simulations, we were able to spatially resolve how proton doping affects the valency of nickel. We also used spatially resolved x-ray nanodiffraction

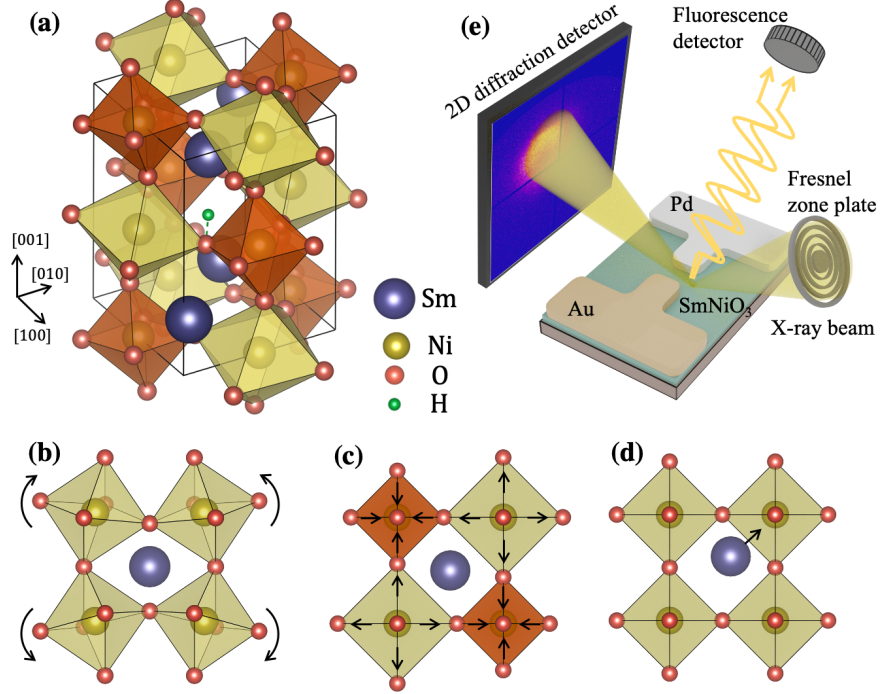


FIG. 1. (a) Orthorhombic crystal structure of SNO. The breathing mode is shown by color: expanded NiO₆ octahedra are yellow and contracted are orange. (b) Schematic representation of the NiO₆ octahedra rotations (tilt pattern) (c) Breathing mode (d) displacement of the rare-earth cation from the centrosymmetric position inside the cavity between NiO₆ octahedra. (e) Scheme of the nanofocused x-ray experiment and the SNO-based device. The focused beam is used for raster scanning of the device where the diffraction signal is recorded by a 2D detector in reflection geometry, and the fluoresce signal is collected by a point energy-resolving detector oriented perpendicular to the sample surface

to reveal the subtle changes in the SNO lattice structure and resolve the correlations to the electronic structure. Despite the wide implementation of ionic motion in many materials, including neuromorphic computing hardware [7], the local measurements of light ion concentrations are very challenging [11]. The experimental results we describe in this work address some of the key questions about the mechanism responsible for resistive changes in nickelate devices doped with light protons.

Pristine SNO has a distorted perovskite structure characterized by corner-connected NiO₆ octahedra with Sm³⁺ ions filling the cavities between the octahedra (Fig. 1(a)). Since the ionic radius of Sm³⁺ is smaller than the size of the cavity, NiO₆ octahedra are tilted [12] and distorted and the rare-earth ions are slightly displaced from the central position (Fig. 1(b)-(d)). The structure can be described by the orthorhombic *Pbnm* symmetry with the unit cell parameters $a_o = 5.328 \text{ \AA}$, $b_o = 5.437 \text{ \AA}$ and $c_o = 7.568 \text{ \AA}$ [13]. Often the pseudocubic crystal

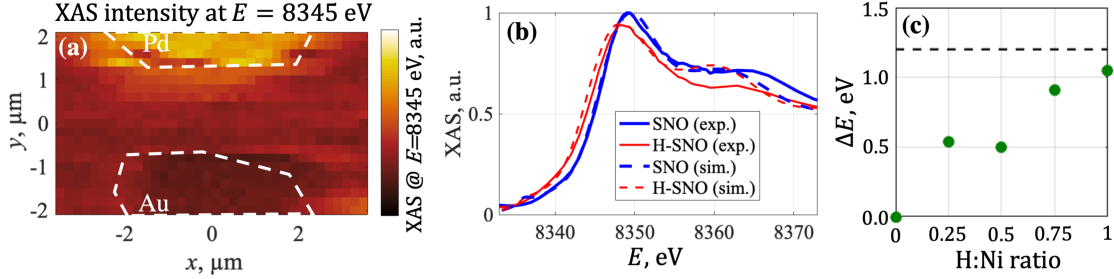


FIG. 2. (a) Spatially resolved map of the fluorescence signal at $E = 8345$ eV. The white dashed lines outline the Pd and Au electrodes. Bright areas next to the Pd electrode correspond to the reduced valence of nickel ions due to the presence of H^+ . (b) Experimentally measured normalized XAS spectra at K-edge of Ni in the pristine SNO away from the Pd electrode and the doped H-SNO under the Pd electrode (solid lines) and FEFF-simulated XAS spectra for the doped H-SNO and undoped SNO (dashed lines). The simulated spectra were additionally convoluted with a Gaussian function to match the same energy resolution as in the experiment. The experimentally observed shift of the XAS spectrum was reproduced in the DFT-simulations at the 1H:1Ni doping level. (c) Dependence of the absorption peak shift ΔE on the concentration of H-dopant for the simulated XAS spectra. Horizontal dashed line marks the experimentally observed value of $\Delta E = 1.2$ eV.

lattice is also used with the unit cell parameters $a_{pc} = b_{pc} = \sqrt{a_o^2 + b_o^2}/2 \approx 3.806$ Å and $c_{pc} = c_o/2 \approx 3.784$ Å [12, 14, 15]. The (101) and (202) orthorhombic reflections considered in this work correspond to the $(\frac{1}{2}\frac{1}{2}\frac{1}{2})_{pc}$ and $(111)_{pc}$ reflections in the pseudocubic notation.

Doping of the SNO with hydrogen decreases its electrical conductivity by eight orders of magnitude [16]. Hydrogen doping means that an extra proton H^+ is implanted in the crystal lattice together with an extra electron e^- to maintain the electrical neutrality. The proposed mechanism has been attributed to the addition of an electron into the system that opens a large gap at the Fermi level [16–18]. A similar effect is observed when SNO is doped with other small ions, such as Li^+ or Na^+ [16, 19]. However, possible changes in the crystal lattice (e.g., the unit cell parameters [11, 17] and the NiO_6 tilt pattern [17, 20]) have been shown to directly influence the conductivity of the nickelates. The goal of this work is to disentangle the effects of electron doping and structural changes with spatial resolution inside a functioning nanodevice.

II. RESULTS

A. Spectroscopy studies of Ni valence

The SNO-based nanodevice [5, 6, 8, 16] and experimental geometry are shown schematically in Fig. 1(e) [21]. Simultaneous diffraction and fluorescence measurements were taken while scanning the focused ~ 30 nm x-ray beam across the device [21]. The spatially resolved fluorescence map near the nickel resonance energy $E = 8345$ eV across the device is shown in Fig. 2(a). This energy corresponds to the highest slope of the x-ray absorption spectrum (XAS), and thus is most sensitive to shifts of the absorption edge caused by a different electronic valency. While the region of the increased fluorescence signal extends several hundred nanometers outside of the Pd electrode, a clear boundary can be resolved near this electrode. This indicates diffusion of H-dopants from the area with the highest dopant concentration directly below the Pd electrode to the pristine SNO film away from the electrode. A comparison of the fluorescence spectra measured between the two electrodes and the region directly under the Pd electrode is shown in Fig. 2(b). A clear shift in the spectra can be seen between these two regions, suggesting an accumulation of dopant in the vicinity of the Pd electrode.

The K-edge transition of Ni corresponds to the promotion of the $1s$ core-level electron into the valence $4p$ shells. The position of the Ni K-edge peak depends on the number of electrons in the Ni $3d$ shells – the decrease of the Ni valence caused by H^+ leads to a shift of the K-edge towards lower energies [22–25]. We experimentally resolved the position of the Ni K-edge by identifying the zero point of the second derivative of the two spectra, which gave us an estimate of 1.2 ± 0.4 eV for the energy shift (Fig. 2(b)).

B. Simulations of $SmNiO_3$ electronic structure

To estimate the corresponding change in the SNO electronic structure (i.e. the Ni oxidation state) [25–27], we simulated the structure of H-SNO using the Vienna *ab initio* simulation package (VASP) [28, 29] and then calculated the theoretical XAS spectra with the FEFF package [30]. In our density-functional theory (DFT) simulations, we tested orthorhombic $Pbnm$ and monoclinic $P2_1/n$ symmetries of SNO, and performed calculations for pristine SNO and doped H-SNO with different atomic ratios of H:Ni.

Our simulations of the low-temperature monoclinic ($P2_1/n$) phase of insulating SNO with known bond-disproportionation exhibits a small band gap of $E_G \approx 0.2$ eV, in agreement with previous publications [14]. A gradual increase in H-doping led to the closing of the band-gap at a 1H:2Ni ratio. A further increase in the doping ratio to 1H:1Ni reopens the band gap to 0.97 eV (five times the undoped band gap) as the structural and electronic properties approach the H-SNO orthorhombic phase at 1H:1Ni doping [21]. This is consistent with the experimental data on H-SNO [6, 16]. This implies that the monoclinic-orthorhombic structural phase transition may occur upon doping, however no discernible bond disproportionation was observed in our diffraction data. Furthermore, the doping ratio required to open a band gap (1H:1Ni) results in an orthorhombic-like configuration in both phases. Consequently, we primarily focused on the orthorhombic phase for this study.

To investigate the influence of the dopant concentration on the electronic structure and electrical properties of H-SNO, we performed the simulations for pristine orthorhombic SNO and four concentration with the 1H:4Ni, 1H:2Ni, 3H:4Ni and 1H:1Ni atomic ratios. This was done by placing a single H-dopant in the $2 \times 2 \times 2$ supercell, $2 \times 1 \times 2$ supercell, conventional unit cell and primitive unit cell, respectively.

The H-dopant inside the SNO unit cell attaches to the oxygen with a bond length of ≈ 1 Å, consistent with the expected bond length of OH^- . There are two nonequivalent oxygen ions to which the H-dopant might be chemically bonded: the basal oxygen in the Ni-O (001) plane and the apical oxygen in the Sm-O (001) plane. Our simulations show that the bonding with the basal oxygen is energetically more favorable by 0.13 eV. This is in agreement with published results [27, 31] showing that, in the stable H-SNO configurations, H-dopant is bonded to the oxygen in the Ni-O planes and occupies the void between the rare-earth cations as shown in Fig. 1(a).

The integrated spin density analysis from the DFT calculations revealed the gradual reduction of the nickel valence from Ni^{3+} in the pristine SNO to Ni^{2+} in the H-SNO at the highest doping level [21]. At the doping level of 1H:1Ni, the band gap of $E_G = 1.14$ eV opens in H-SNO, indicating the very high resistivity of the hydrogenated H-SNO [16, 27], while no band gap is observed at lower doping level (3H:4Ni and below [21]).

The DFT simulations were performed in two regimes: with the fixed values of the lattice parameters and with volume relaxation. In the latter case we observed a $\sim 10\%$ increase in the value of b_o lattice parameter under a 1H:2Ni dopant ratio, in line with the previous

computational results [32]. However, the reduction of nickel oxidation remains consistent with and without volume relaxation. As such, we simulated the XAS spectra of H-SNO with a fixed lattice to maintain consistency with our diffraction results whereby the plane strain in SNO is confined by the interface with the LAO substrate. The theoretical XAS spectra for SNO and H-SNO calculated with the FEFF package [30] are shown in Fig. 2(b) and exhibit the same shift $\Delta E_{DFT} \approx 1.05$ eV as was observed in the experiment.

Using the results of the DFT simulations as an input for FEFF software [30], we calculated the XAS spectra of the Ni K-edge for various doping level (Fig. 2(b)) and observed a gradual shift of the absorption edge with the dopant concentration. Our simulation confirms that this shift increases with doping concentration as shown in Fig. 2(c). This allowed us to estimate the doping level to be at the atomic ratio of about 1H:1Ni in our experiment. Furthermore, the shifting of the absorption peak to a lower energy in H-SNO (Fig. 2(b)) is qualitatively consistent with the shift in the XAS spectrum for NiO (valence state of Ni²⁺) to a lower energy with respect to Ni₂O₃ (valence state of Ni³⁺) [21]. Moreover, our DFT simulations indicated that only this high doping level leads to opening of the band gap, while at lower concentrations the nickelate film remains conductive. This means that the bright region next to the Pd electrode (Fig. 2(a)) with the doping level close to 1H:1Ni ratio corresponds to the insulating phase which determine the electrical properties of the nickelate nanodevice [5, 33].

C. Changes in SmNiO₃ crystal structure

The changes of the crystal structure in the nanodevice upon H⁺ doping can be studied by considering the spatially resolved maps of the diffraction signal. In Fig. 3(a) the intensity of the (101) reflection is shown measured on a second device. The striking feature of this map is the dark region below the Pd electrode which extends over more than 1 μm towards the Au electrode. The intensity in this region is approximately four times smaller than under the Au electrode. However, the Q -position of the (101) and (202) reflections changes over less than 0.35 % across the device, indicating that the lattice parameters did not change for the doping levels studied here (Fig. 3(b)). Also no gradual changes in the doped region can be seen in Fig. 3(c), where the intensity of (202) reflection is shown. Our combined experimental and simulation results strongly suggest a weaker role of the lattice in generating the changes in

resistance [11].

To demonstrate that a little rearrangement of the atoms within the unit cell can cause a change of the diffraction peak intensity, we calculated the x-ray diffraction from a perovskite structure. The intensity of a Bragg reflection is proportional to the squared modulus of the form factor

$$I(\mathbf{q}) \propto |F(\mathbf{q})|^2 = \left| \sum_j O_j f_j(q) \exp(i\mathbf{q}\mathbf{r}_j) \right|^2, \quad (1)$$

where \mathbf{q} is a scattering vector, index j numerates atoms in the unit cell (see Fig. 1(a), O_j is occupancy, $f_j(q)$ is atomic form factor, and \mathbf{r}_j is the position of each atom. In the ideal perovskite structure (i.e. without tilts and distortions of the NiO_6 octahedra as well as displacement of the rare-earth cation), the orthorhombic (101) reflection is forbidden, i.e., the contribution from different atoms in Equation (1) cancel out. The deviations from the ideal structure in pristine SNO that result in the non-zero intensity of the (101) reflection are shown in Fig. 1(b)-(d) and include NiO_6 octahedra rotations [12], Ni-O bond disproportionation (breathing of the NiO_6 octahedra) [34–36], and displacement of the rare-earth cations [37].

In order to understand the individual contributions to the intensity of the (101) reflection, we considered a model of the SNO structure [21]. The oxygen ions form ideal octahedra around the nickel ions where the length of the Ni-O bond is $d_{\text{Ni-O}} = d_{\text{Ni-Ni}}(1 \pm B)/2$; here $d_{\text{Ni-Ni}}$ is the distance between two Ni^{3+} ions and $B \approx 1.3\%$ is the magnitude of the breathing mode [35, 38]. The alternating expanded and contracted octahedra form a three-dimensional checkerboard pattern [14, 35]. Furthermore, each NiO_6 octahedron is rotated about the [100], [010], and [001] directions in the orthorhombic unit cell [39] over angles α , β , and γ to form the tilt pattern inherent to rare-earth nickelates [12]. In this orthorhombic notation, the rotations $\alpha = 0^\circ$, $\beta = 15.26^\circ$, and $\gamma = 7.9^\circ$ correspond to the reported values of the Ni-O-Ni angles $\theta_{ap} = 149.5^\circ$ and $\theta_b = 154.2^\circ$ for the apical and basal oxygen atoms, respectively [13, 40]. The displacement of Sm^{3+} ions from the symmetric position between the NiO_6 octahedra was described by three parameters, d_x , d_y , and d_z , corresponding to the shift along the [100], [010], and [001] orthorhombic directions (Fig. 1(a)). In pristine SNO, the values of d_x and d_y are reported to be 0.06 Å and 0.28 Å, while d_z equals zero [13, 41].

Because of the twinning ($a_o \approx b_o$), the intensity measurement of the (101) reflection accounts for the contribution from (101), $(10\bar{1})$, (011), and $(01\bar{1})$ [41]. Therefore, in our

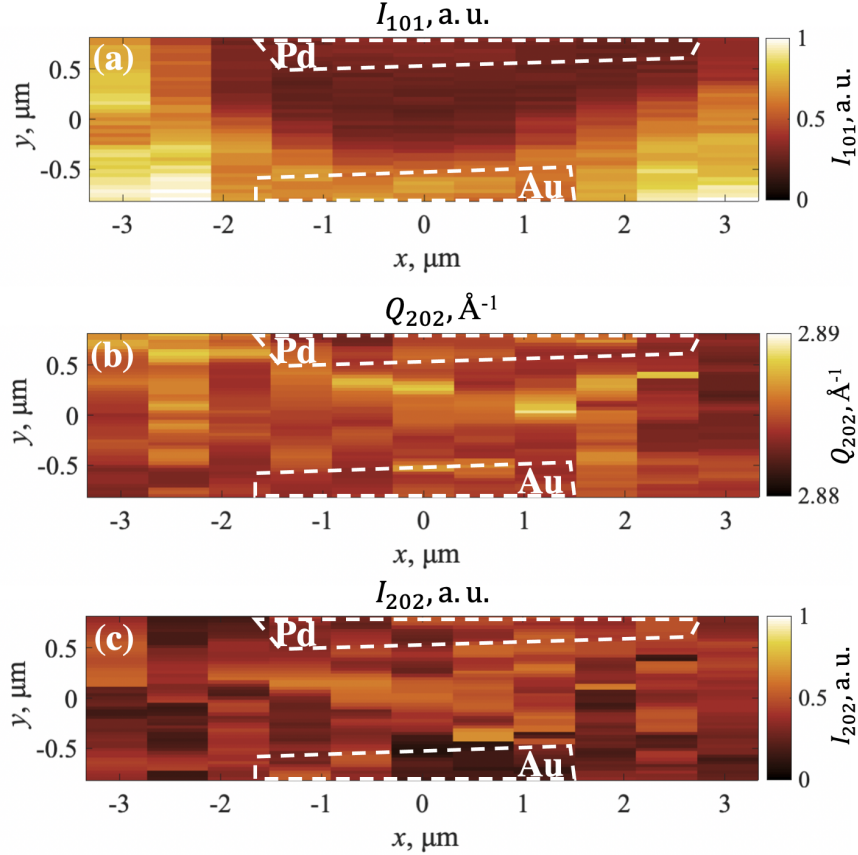


FIG. 3. (a) Normalized intensity map of the (101) reflection. The white dashed lines outline Pd and Au electrodes. The dark region between the electrodes corresponds to the area where H^+ doping results in structural changes in the film. (b) Spatially-resolved map of the Q -position (\AA^{-1}) of the (202) reflection. (c) Normalized intensity map of the (202) reflection.

diffraction simulations we calculated the averaged intensity of these four reflections; and the similar procedure was performed for the (202) peak. We varied the values of the above-listed distortions of the orthorhombic crystal lattice around the values reported for pristine SNO by the following amounts: $\Delta\alpha, \Delta\beta, \Delta\gamma = \pm 2^\circ$, $B = 0 - 3\%$, and $\Delta d_x, \Delta d_y, \Delta d_z = \pm 0.3 \text{\AA}$. Our calculations show that the averaged intensity of the (101) reflection is determined mainly by the displacement of the rare-earth cation, while the combined contribution from the breathing mode and tilt pattern constitutes only $\sim 5\%$ of the total intensity (Fig. 4(a)-(c)). This can be understood since the two latter effects include movement of oxygen atoms that are weak x-ray scatters ($|f_{\text{O}^{2-}}|/|f_{\text{Sm}^{3+}}| \sim 0.1$ at $E = 8345 \text{ eV}$); however, strictly speaking, this argument is valid only for the (101) reflection [41]. The intensity of the (202) reflection almost does not change upon considered deviations from the ideal perovskite structure (Fig. 4(d)-(f)).

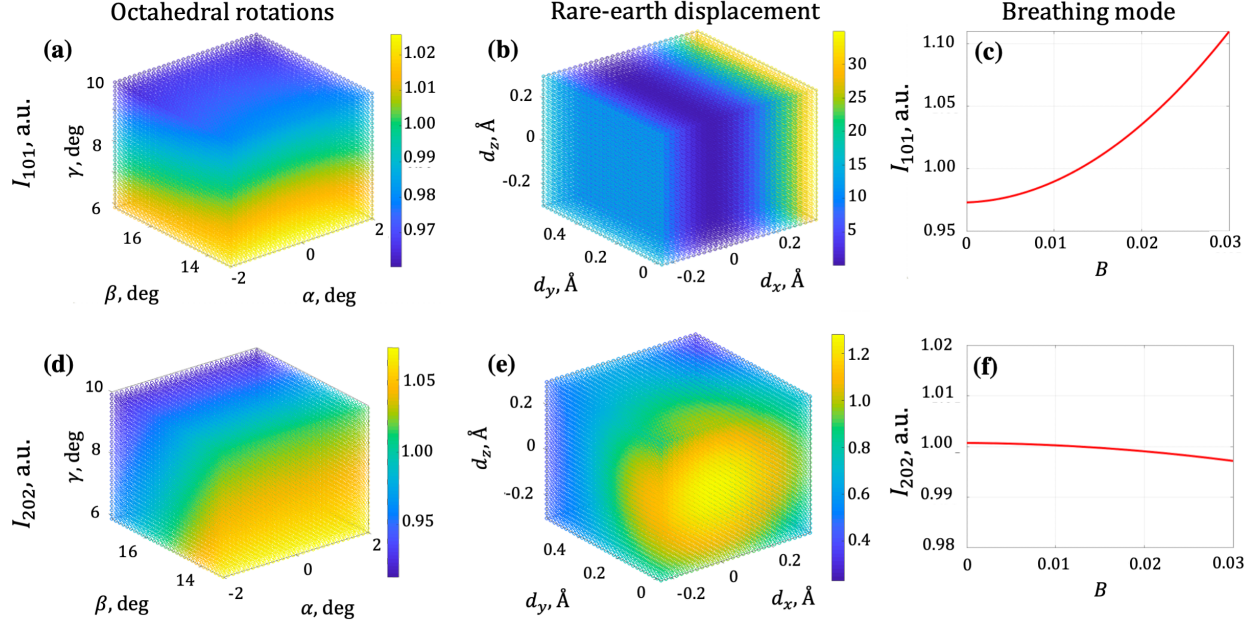


FIG. 4. (a-c) Simulated intensity the (101) reflection and (d-f) intensity of the (202) reflection as a function of NiO₆ octahedra tilt angles α , β , γ (a,d), the displacement of the Sm³⁺ cation d_x, d_y, d_z (b,e), and the breathing distortion B (c,f). The intensities I_{101} and I_{202} are normalized to the value in the pristine SNO.

Neglecting the contribution from oxygen ions in Equation (1), the intensity of the averaged (101) reflection depends only on the cation displacements along [100] and [001] directions [21]

$$I_{101} \propto \exp \left[- \left(\frac{2\pi\sigma_x}{a_o} \right)^2 - \left(\frac{2\pi\sigma_z}{c_o} \right)^2 \right] \sin^2 \frac{2\pi d_x}{a_o} \cos^2 \frac{2\pi d_z}{c_o}. \quad (2)$$

Here σ_x and σ_z are the root-mean-square displacement of the Sm³⁺ ions along the [100] and [001] directions from the equilibrium positions dictated by d_x and d_z . In pristine SNO, $\sigma_x \sim \sigma_z \sim 0.05 \text{ \AA}$. The dependence of the (101) reflection intensity on σ_x , σ_z , d_x , and d_z is shown in Fig. 5(a)-(b), to illustrate the combined impact of each parameter in Equation (2). The strongest decrease of the (101) reflection intensity is caused by the shift of the Sm³⁺ cations towards the symmetric position along the [100] direction (i.e., $d_x \rightarrow 0$). Meanwhile, in our calculations the intensity and the position of the (202) reflection remains practically constant, which coincides with the experimental x-ray data (Fig. 3(b)-(c)).

The one-to-one correspondence also allows one to directly map the intensity of the (101) reflection into the displacement of the rare-earth cation. In Fig. 5(c), the intensity of the (101) is plotted with the corresponding variation of the displacement parameter d_x shown along the $x = 0$ line cut of the intensity map (Fig. 3(a)). The proportionality coefficient

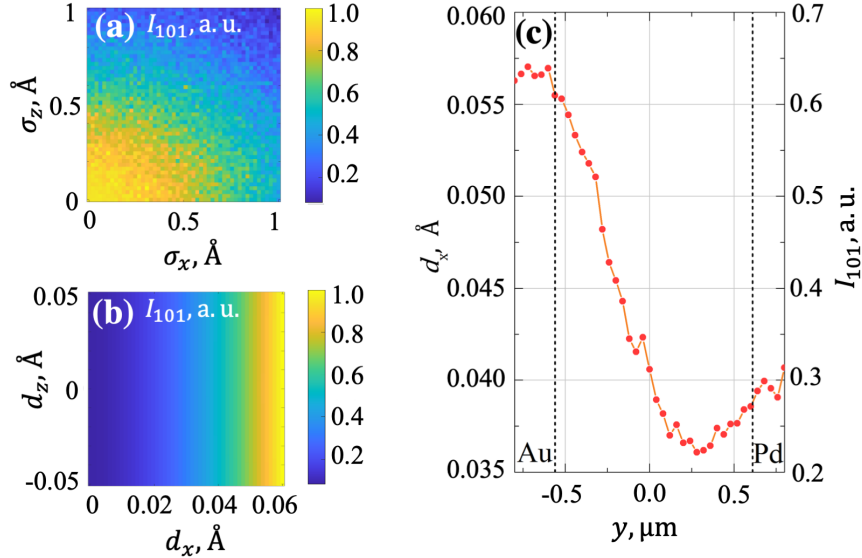


FIG. 5. (a-b) Dependence of the (101) peak intensity on the root-mean-square displacement (a) and mean position of the Sm^{3+} ions (b). The intensity was evaluated by fixing the positions of all ions in the SNO unit cell and allowing only Sm^{3+} to move. For each value of the parameters the result was statistically averaged over 10^4 realizations. (c) Mean shift of the Sm^{3+} ions and the corresponding change of intensity along the $x = 0$ line in the spatially resolved map in Fig. 3(a) using Equation 2. Vertical lines mark Au and Pd electrodes.

between intensity and d_x was determined by assigning the maximum intensity of the (101) peak below the Au electrode to the literature values of SNO ($d_x \approx 0.06$ Å). The outstanding feature of this plot is a non-monotonic change of the d_x parameter between the electrodes: the minimum value of d_x is reached approximately 250 nm away from the Pd electrode. This suggests that the diffusion coefficient of H^+ in SNO may depend on H^+ concentration, which leads to accumulation and stagnation of dopants next to the catalytic Pd electrode. This also shows that H^+ doping can affect the structure of SNO up to 1 μm away from the Pd electrode, where the protons were initially introduced. This information is important for optimization of the electrode shape and scaling of the device and requires a dedicated investigation. Finally, our results are in agreement with own DFT calculations and published works [27, 31] which predict that the H-dopant occupies the void next to the rare-earth cation and can cause its displacement sufficient to decrease the intensity of the (101) reflection.

III. DISCUSSION

At first glance, the shift of the rare-earth cation towards the centrosymmetrical position in the unit cell and the decrease of the oxygen octahedra rotations seem to be a counter-intuitive result of the H^+ implantation, because these structural changes actually make the SNO crystal lattice closer to the ideal perovskite structure. On the other hand, the rare-earth nickelates with large rare-earth cations are known to have less distorted crystal structures (i.e., exhibit smaller octahedral tilts), than the nickelates with small cations [14]. Therefore, implantation of H^+ next to the rare-earth cation may effectively increase the radius of the latter, which would result in a decrease of the NiO_6 tilt angles, causing the system to be more metallic. We should also note that, even with our spatial resolution, our probe measures an average structure across the beam footprint. This means that the implanted H^+ can produce local lattice defects and distortions within a unit cell that cannot be measured by x-ray diffraction (as it is shown in Fig. 5(a)). A hint that these local distortions are averaged out in diffraction can be seen in the slight broadening of the H-SNO absorption spectra as compared to the pristine SNO (Fig. 2(b)).

Together, our data suggest that the dramatic changes in resistance upon hydrogenation come from the change in electronic valency, not from structural distortions. This is also supported by further DFT simulations, in which we considered separately the structural and electronic effects of H-doping [21]. More specifically, we added an H atom to the SNO and allowed the structure to relax under the following constrains: a) only H doping, no crystal structure relaxation (positions of Sm, Ni and O are fixed); b) only structural changes (positions of Sm, Ni and O are as in the H-SNO), but no H doping; c) H doping and Sm relaxation (only Sm atoms were allowed to move); d) H doping and NiO_6 relaxation (only O atoms were allowed to move). In result, we found that the pure structural changes do not lead to the band gap opening, while just the H-doping without the structural relaxation lead to the formation of the band gap $E_G \approx 0.5$ eV. In addition, the relaxation of the NiO_6 octahedra increases the band gap to $E_G \approx 1.0$ eV. In all cases, the opening of the band gap is accompanied by the reduction of nickel from Ni^{3+} to Ni^{2+} [21]. These simulations confirms that the origin of the insulating properties of H-SNO lies in electron doping, while the structural changes play only the second role.

These simulations show that mere structural changes do not cause a band gap opening,

while only change in nickel valence (without structural relaxation) already causes the opening of a band gap. Therefore, the insulating properties of H-SNO arise primary from the change of Ni valence, while subtle changes in the crystal structure (mostly within the NiO_6 octahedra) further increase the band gap to its final value.

In the diffraction, we are mostly sensitive to the displacement of the Sm^{3+} cations, which we indeed observed in our experiment (Fig. 3(a)), while other structural changes could not be directly detected in our data. This gives us only indirect information on the changes in SNO crystal lattice. For example, the rare-earth cation displacement is known to be coupled with the tilt of the NiO_6 octahedra [37], so possibly a change in the NiO_6 rotation also takes place with hydrogenation. However, we anticipate that the rotation angles of the NiO_6 octahedra are only slightly decreased with hydrogenation, based on the small value of Sm^{3+} displacement that we observe experimentally. This further suggests that hydrogenating other transition metal oxides with different crystal structures might also yield changes in resistance.

In summary, we used a nanofocused x-ray beam to perform spatially resolved spectroscopic and structural studies of a H-SNO-based nanodevice. As a result of H^+ doping, we observed the 1.2 eV shift of the Ni K-edge towards lower energies. Our DFT simulations account for this shift by estimating a reduction of the nickel valence from Ni^{3+} to Ni^{2+} at the 1H:1Ni doping level. We also observed the decrease of the (101) Bragg peak intensity next to the Pd electrode. Structural modeling revealed that this can be caused by a shift of the Sm^{3+} cations over $\sim 0.03 \text{ \AA}$ towards the centrosymmetrical position inside the voids between the NiO_6 octahedra. This displacement of rare earth cations is usually neglected, when the unit cell of the SNO is approximated by pseudocubic structure. Combining the x-ray spectroscopy and diffraction data, we elucidate how H^+ doping changes the structure and electronic properties of an SNO device. Our methods also pave the way for future x-ray nanoscale studies of devices based on transition metal oxides.

IV. METHODS

A. Sample preparation

The SNO-based nanodevices studied here consist of a 150 nm thick SNO film epitaxially grown with a high vacuum sputtering system on (111)_{pc}-oriented LaAlO₃ substrate [5]. This orientation was chosen such as to be able to access Bragg peaks associated with octahedral distortions of the kind (101) [40–42]. Two 5 μm -wide electrodes of Pd and Au were fabricated over the film with a lateral gap of 1 – 2 μm using e-beam lithography. The thickness of the electrodes next to the gap was 50 nm. The Pd electrode served as a catalyst to split H₂ molecules and incorporate H⁺ in the SNO film during annealing for 5 minutes at 120 °C in the H₂/N₂ mixture (5%/95%) [5, 8, 16, 17].

B. X-ray nanofocusing experiments

The nanofocused x-ray experiments were performed at the 26-ID-C beamline of the Advanced Photon Source (APS) and 3-ID beamline of the National Synchrotron Light Source II (NSLS II) [43, 44], using photons with energy of 8315-8385 eV to measure the fluorescence around the Ni K-edge near 8345 eV at room temperature [21]. At this energy, the resolution was about 0.5 eV achieved by a double-crystal monochromator. The XAS data were taken using a fluorescence detector placed above the device [45]. The diffraction data were acquired with a two-dimensional photon counting detector with 55 μm pixels oriented perpendicular to the diffracted beam. A Fresnel zone plate was placed upstream from the sample to focus the beam down to ~ 30 nm at the sample. To collect the spatially resolved diffraction and fluorescence data, the sample was raster-scanned with the nanofocused x-ray beam. The Au and Pd contacts served as fiducials to easily locate the device using their fluorescence.

C. DFT simulations

All DFT calculations [46, 47] were performed using the Vienna Ab initio Simulation package (VASP) [28] within the projector augmented wave (PAW) approach [21, 48]. The exchange-correlation effects were modeled using the Perdew-Berke-Ernzerhof (PBE) gener-

alized gradient approximation (GGA) [49] functional under the Hubbard correction with $U = 2$ eV [31, 50]. We used a plane wave cutoff energy of 520 eV with the energies and atomic forces converged to within 10^{-4} eV and -0.02 eV/Å respectively. All analysis and input generation was performed with the aid of the Python Materials Genomics (pymatgen) package [51]. We performed full relaxation for the pristine and H-doped structures of SmNiO_3 and all calculations were spin-polarized.

We modeled the pristine and H-doped SmNiO_3 system using the metallic orthorhombic ($Pbnm$) phase. SmNiO_3 is known to be paramagnetic [14], however DFT is only able to simulate magnetically ordered phases (e.g., ferromagnetic (FM) and antiferromagnetic (AFM)) or non-magnetic (NM) phases. As such we investigated both the FM and AFM phases.

ACKNOWLEDGMENTS

This work was supported as part of Quantum Materials for Energy Efficient Neuromorphic Computing (Q-MEEN-C), an Energy Frontier Research Center funded by the U.S. Department of Energy (DOE), Office of Science, Basic Energy Sciences (BES), under Award # DE-SC0019273. X-ray microscopy measurements were supported by the DOE, Office of Science, BES, under Contract # DE-SC0001805. Research at the Center for Nanoscale Materials and the Advanced Photon Source, both Office of Science user facilities, was supported by the DOE, Office of Science, BES, under contract # DE-AC02-06CH11357. Research at the Hard X-ray Nanoprobe Beamline of sector 3-ID of the National Synchrotron Light Source II was supported by the DOE Office of Science under contract # DE-SC0012704 and is operated by Brookhaven National Laboratory.

Supplemental Materials: SNO device fabrication and characterization

The devices studied here consist of a 150 nm SNO film on LAO substrate with the two 50 nm thick contacts of Au and Pd fabricated on top of the SNO film. The geometry of the device is schematically shown in Figure **Figure S1a**. In this work, we used two types of devices with a 1 μm and 2 μm gap between the Au and Pd contacts. Both devices have similar electrical properties and exhibit a colossal increase in resistance, as it is shown in Figure **Figure S1b,c**.

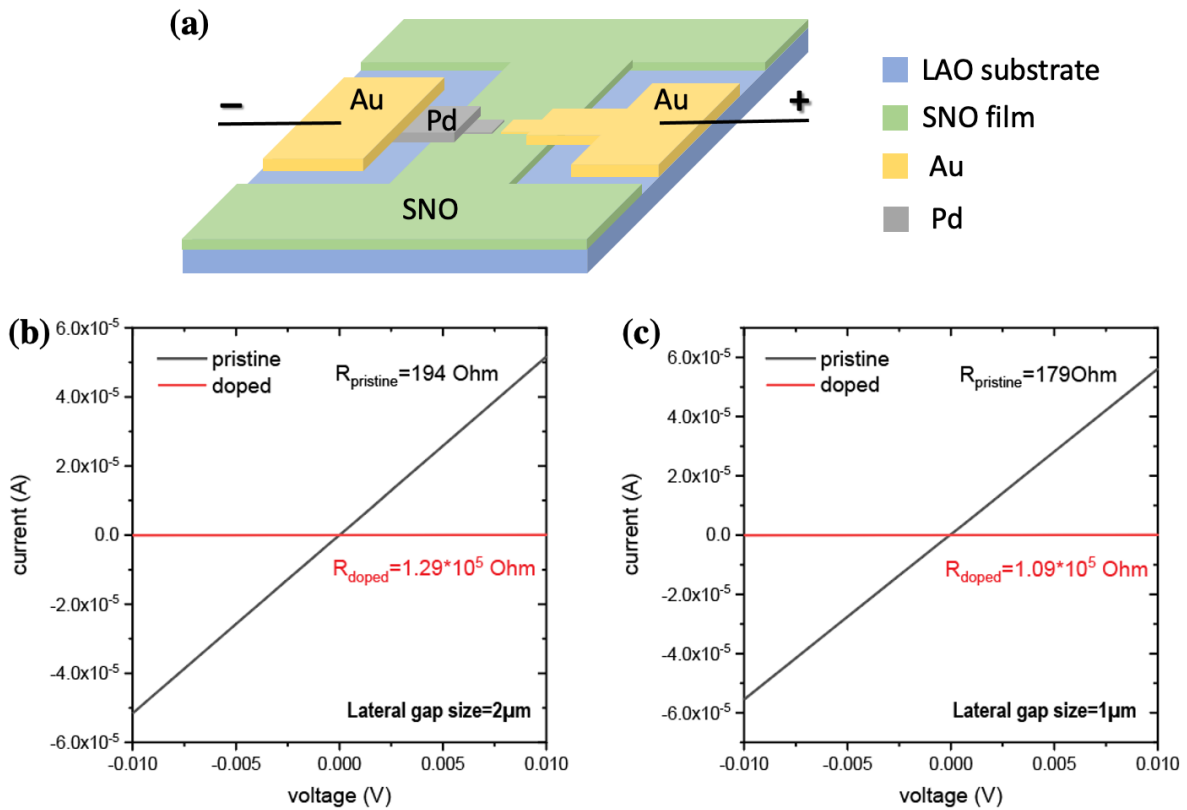


FIG. S1. (a) Scheme of the fabricated SNO device. (b-c) Representative data taken from two different SNO devices showing resistance modulation due to hydrogen doping. (a) Current (I) - voltage (V) characterization between -10mV to +10mV collected from a device with a 2 μm lateral gap size. The fitted slopes indicated the resistance before doping (pristine) was 194 Ohm and after doping was 129 kOhm. (b) Current (I) - voltage (V) characterization between -10mV to +10mV collected from a device with a 1 μm lateral gap size. The fitted slopes indicated the resistance before doping (pristine) was 179 Ohm and after doping was 109 kOhm. The resistance increases in both cases after hydrogen doping due to the electron transfer from the hydrogen to the nickel orbitals, opening up a transport gap. The device structure and fabrication process are detailed in the main text. The samples were annealed in H_2/Ar (5%/95%) forming gas at 120 $^\circ\text{C}$ for 10 minutes for the doping process.

Supplemental Materials: Spatially resolved diffraction studies

The SNO-based memory device was scanned with a nanofocused x-ray beam with an exposure time of 10 s for (101) peak and 1 s for (202) peak. A Fresnel zone plate was placed upstream from the sample to focus the beam down to ~ 30 nm at the sample. The footprint of the x-ray beam for the (101) peak was approximately 170×30 nm² (hor. \times vert.), and for the (202) peak – 90×30 nm². At the 26-ID-C beamline (APS) the zone plate optics was moved in order to ensure stability of the sample during the scan. At the 3-ID beamline (NSLS-II) the sample was moved with respect to the x-ray beam, while the stability was ensured through the high stiffness design of the microscope sample stage. The XAS data were taken using a fluorescence detector placed above the device [45]. The diffraction data were acquired with a two-dimensional photon counting detector with 55 μ m pixels oriented perpendicular to the diffracted beam. The averaged diffraction patterns are shown in **Figure S2a,b**. The scattering angle 2θ increases from right to left and the

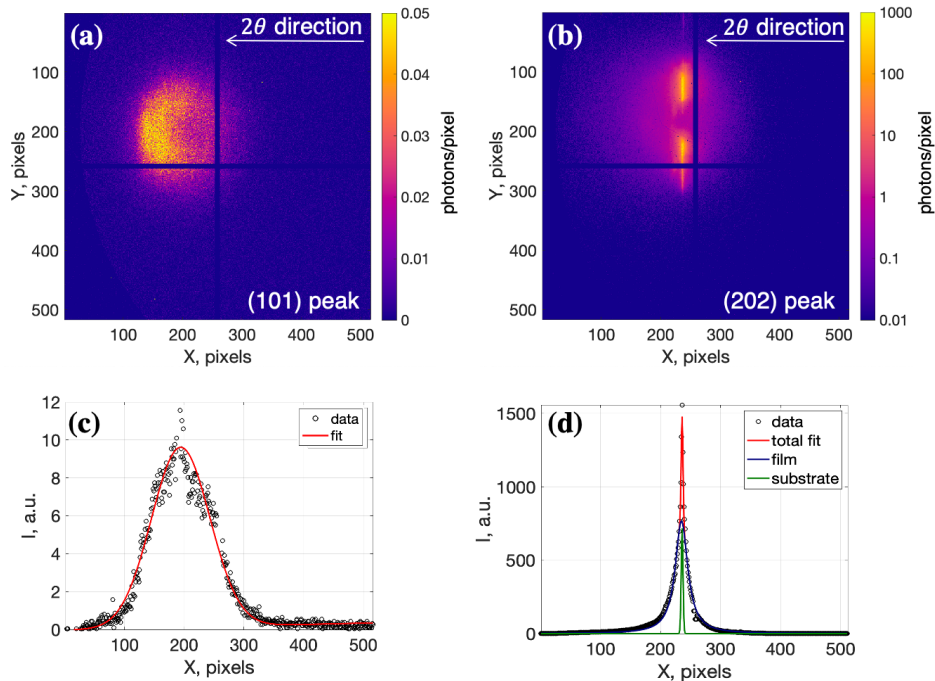


FIG. S2. Averaged diffraction pattern for the (101) reflection (a) and the (202) reflection (b). Projection of the averaged diffraction pattern along the vertical direction is shown in (c,d). The signal from the (101) reflection can be fitted by a single Gaussian function (c), while the signal from the (202) reflection can be approximated by a sum of the Lorentzian and Gaussian functions corresponding to the scattering from the SNO film and the LAO substrate, respectively (d).

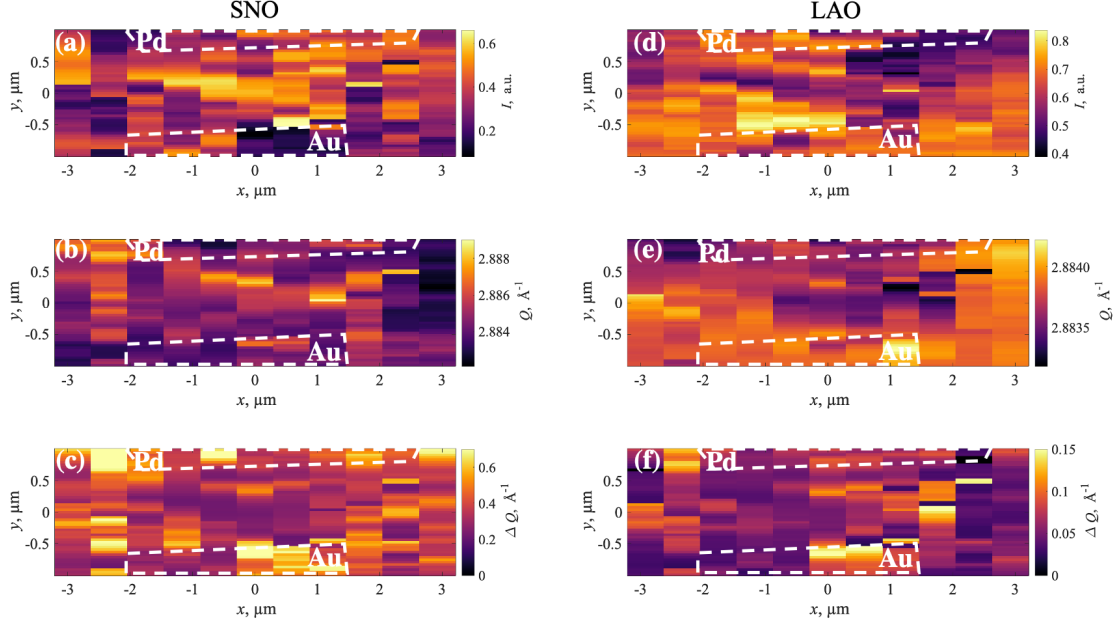


FIG. S3. (a-c) Intensity (a), Q -position (b), and the width (c) of the (202) reflection from the SNO film. (d-f) Intensity (d), Q -position (e), and the width (f) of the LAO (111) substrate reflection. The electrodes are outlined with dashed lines.

dispersion along the vertical direction is due to the Fresnel zone plate used for focusing. The projected signal along the 2θ -direction is shown in **Figure S2c,d**.

In **Figure S3** spatially resolved maps of the intensity, position and width of the (202) reflection from the SmNiO_3 (SNO) film and the $(111)_{pc}$ reflection from the LaAlO_3 (LAO) substrate are shown. These maps show no changes of the unit cell parameters induced by H^+ doping. In contrast to that, the intensity of the (101) reflection is about four times dimmer in the proton-doped region next to the Pd electrode (see **Figure 3a** in the main text). The variations of intensity in **Figure S3a,d** are attributed to the heterogeneity of the substrate and almost complete overlap between the film and substrate peaks, which did not allow to reliably separate two signals (see **Figure S2c,d**).

The position of electrodes was determined using the Au and Pd fluorescence signal, as shown in **Figure S4a,b**. The thickness of the electrodes next to the gap was 50 nm. The Ni fluorescence map at $E = 8395$ eV (away from the K-edge resonance, hence not sensitive to the valence state of nickel) shows that the SNO film is uniform. A small absorption of the Ni fluorescence signal under the electrodes can be noticeable in **Figure S4d**, but it has a neglectable effect on the position of the Ni K-edge.

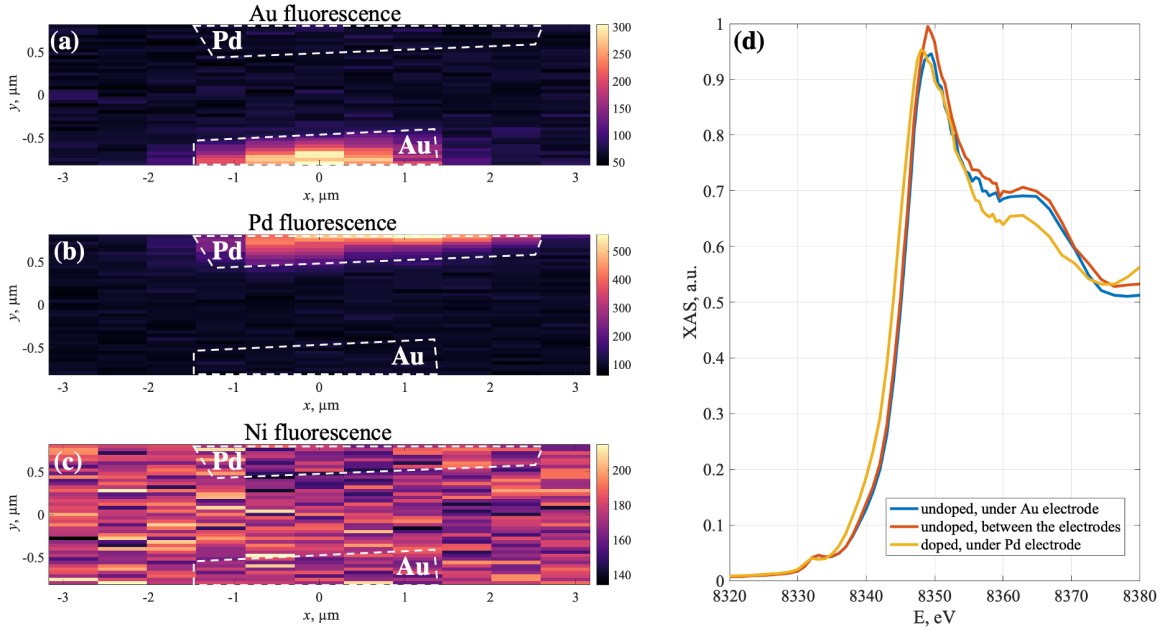


FIG. S4. (a-b) Fluorescence signal from Au (a) and Pd (b) indicates position of electrodes. (c) Non-resonant fluorescent signal from Ni shows the uniform SNO film across the device. (d) XAS spectra at Ni K-edge taken under the Au and Pd electrodes and in the middle of the gap between the electrodes.

Supplemental Materials: Simulation of x-ray diffraction

1. SmNiO_3 perovskite crystal lattice

An orthorhombic unit cell of a perovskite SNO lattice was constructed in several steps. In our analysis, we assumed that Ni atoms do not move with hydrogen doping, so the positions of the twelve Ni atoms was fixed within a unit cell. Then four Sm atoms were placed inside a unit cell and allowed to be shifted from the centrosymmetric positions over d_x , d_y , and d_z in such a way, that the orthorhombic $Pbnm$ symmetry was preserved. Finally, we placed six O atoms in the corners of octahedra centered at every Ni atom (twenty oxygen atoms in total, if counting only atoms within a unit cell) and took the tilt and breathing distortion of the NiO_6 octahedra into account. To achieve that, the position of each oxygen atom was calculated according to the following procedure:

1. For each oxygen atom, a nesting nickel atom was selected, around which the rotations will be performed.

2. The position of the oxygen atom was calculated as

$$\mathbf{r}_O = \mathbf{r}_{Ni} + \tilde{\mathbf{u}} , \quad (\text{S1})$$

where $\mathbf{r}_O = (x_O, y_O, z_O)$ are coordinates of the oxygen atom and $\mathbf{r}_{Ni} = (x_{Ni}, y_{Ni}, z_{Ni})$ are coordinates of the corresponding nickel atom. The relative coordinates $\tilde{\mathbf{u}} = (\tilde{x}, \tilde{y}, \tilde{z})$ were calculated as

$$\tilde{\mathbf{u}} = (1 \pm B) \cdot \hat{R}(\pm\alpha, \pm\beta, \pm\gamma)\mathbf{u}_0 . \quad (\text{S2})$$

Here $\mathbf{u}_0 = (x_0, y_0, z_0)$ are the relative coordinates of the oxygen atom in an ideal perovskite structure (in which each oxygen atom is located exactly in the middle between two nickel atoms), $\hat{R}(\alpha, \beta, \gamma)$ is an operator of rotation over the angles α , β and γ about x -, y - and z -axis, correspondingly, and the pre-factor $(1 \pm B)$ takes the breathing distortion with a magnitude B into account (plus sign corresponds to the expanded NiO_6 octahedra, and minus sign – to the contracted).

3. The signs of rotation angles α , β and γ for each octahedra are selected in such a way that the final structure corresponds to the $a^-a^-c^+$ tilt pattern in Glazer notation [12].

We assigned an occupation number O_j to each atom, which takes into account that the atom might be shared between several neighboring unit cells. For example, $O_j = 1$ for an atom that is completely inside a unit cell, while $O_j = 1/4$ for an atom placed on the edge of a unit cell, since this atom is shared between four adjacent unit cells.

The parameters of the structural model are summarized in **Table I**. The first column contains an index of an atom j , the second column – type of an atom. Columns 3–5 contains coordinates x , y and z of an atom, and column 6 – occupation number O_j . For each Ni atom the signs of rotation angles α , β and γ and the breathing distortion are specified in columns 7 and 8, respectively (this information is duplicated for each oxygen atom). The values of $\tilde{\mathbf{u}} = (\tilde{x}, \tilde{y}, \tilde{z})$ for each oxygen atom are calculated with **Equation S2**, using the undistorted coordinates $\mathbf{u}_0 = (x_0, y_0, z_0)$ specified in columns 9–11. The crystal structure of pristine SNO constructed with our model using the parameter values $\alpha = 0^\circ$, $\beta = 15.26^\circ$, and $\gamma = 7.9^\circ$, $d_x = 0.06 \text{ \AA}$, $d_y = 0.28 \text{ \AA}$, $d_z = 0 \text{ \AA}$, and $B = 0.013$ coincides with the literature data [13, 34] (see **Figure S5**).

#j	Atom	x_j	y_j	z_j	O_j	Rotation	Breathing	x_0	y_0	z_0
1	Ni	$a_o/2$	0	0	1/4	--+	+			
2	Ni	0	$b_o/2$	0	1/4	++-	-			
3	Ni	$a_o/2$	b_o	0	1/4	--+	+			
4	Ni	a_o	$b_o/2$	0	1/4	++-	-			
5	Ni	$a_o/2$	0	$c_o/2$	1/2	+++	-			
6	Ni	0	$b_o/2$	$c_o/2$	1/2	----	+			
7	Ni	$a_o/2$	b_o	$c_o/2$	1/2	+++	-			
8	Ni	a_o	$b_o/2$	$c_o/2$	1/2	----	+			
9	Ni	$a_o/2$	0	c_o	1/4	--+	+			
10	Ni	0	$b_o/2$	c_o	1/4	++-	-			
11	Ni	$a_o/2$	b_o	c_o	1/4	--+	+			
12	Ni	a_o	$b_o/2$	c_o	1/4	++-	-			
13	Sm	$a_o - d_x$	d_y	$c_o/4 + d_z$	1					
14	Sm	$a_o/2 + d_x$	$b_o/2 + d_y$	$c_o/4 + d_z$	1					
15	Sm	$a_o/2 - d_x$	$b_o/2 - d_y$	$3c_o/4 - d_z$	1					
16	Sm	d_x	$b_o - d_y$	$3c_o/4 - d_z$	1					
17	O (1)	$a_o/2 + \tilde{x}$	\tilde{y}	\tilde{z}	1/2	--+	+	$a_o/4$	$b_o/4$	0
18	O (1)	$a_o/2 + \tilde{x}$	\tilde{y}	\tilde{z}	1/2	--+	+	0	0	$c_o/4$
19	O (2)	\tilde{x}	$b_o/2 + \tilde{y}$	\tilde{z}	1/2	++-	-	$a_o/4$	$-b_o/4$	0
20	O (2)	\tilde{x}	$b_o/2 + \tilde{y}$	\tilde{z}	1/2	++-	-	$a_o/4$	$b_o/4$	0
21	O (2)	\tilde{x}	$b_o/2 + \tilde{y}$	\tilde{z}	1/2	++-	-	0	0	$c_o/4$
22	O (3)	$a_o/2 + \tilde{x}$	$b_o + \tilde{y}$	\tilde{z}	1/2	--+	+	$a_o/4$	$-b_o/4$	0
23	O (3)	$a_o/2 + \tilde{x}$	$b_o + \tilde{y}$	\tilde{z}	1/2	--+	+	0	0	$c_o/4$
24	O (4)	$a_o + \tilde{x}$	$b_o/2 + \tilde{y}$	\tilde{z}	1/2	++-	-	0	0	$c_o/4$
25	O (5)	$a_o/2 + \tilde{x}$	\tilde{y}	$c_o/2 + \tilde{z}$	1	+++	-	$a_o/4$	$b_o/4$	0
26	O (5)	$a_o/2 + \tilde{x}$	\tilde{y}	$c_o/2 + \tilde{z}$	1/2	+++	-	0	0	$c_o/4$
27	O (6)	\tilde{x}	$b_o/2 + \tilde{y}$	$c_o/2 + \tilde{z}$	1	----	+	$a_o/4$	$-b_o/4$	0
28	O (6)	\tilde{x}	$b_o/2 + \tilde{y}$	$c_o/2 + \tilde{z}$	1	----	+	$a_o/4$	$b_o/4$	0
29	O (6)	\tilde{x}	$b_o/2 + \tilde{y}$	$c_o/2 + \tilde{z}$	1/2	----	+	0	0	$c_o/4$
30	O (7)	$a_o/2 + \tilde{x}$	$b_o + \tilde{y}$	$c_o/2 + \tilde{z}$	1	+++	-	$a_o/4$	$b_o/4$	0
31	O (7)	$a_o/2 + \tilde{x}$	$b_o + \tilde{y}$	$c_o/2 + \tilde{z}$	1/2	+++	-	0	0	$c_o/4$
32	O (8)	$a_o + \tilde{x}$	$b_o/2 + \tilde{y}$	$c_o/2 + \tilde{z}$	1/2	----	+	0	0	$c_o/4$
33	O (9)	$a_o/2 + \tilde{x}$	\tilde{y}	$c_o + \tilde{z}$	1/2	--+	+	$a_o/4$	$b_o/4$	0
34	O (10)	\tilde{x}	$b_o/2 + \tilde{y}$	$c_o + \tilde{z}$	1/2	++-	-	$a_o/4$	$-b_o/4$	0
35	O (10)	\tilde{x}	$b_o/2 + \tilde{y}$	$c_o + \tilde{z}$	1/2	++-	-	$a_o/4$	$b_o/4$	0
36	O (11)	$a_o/2 + \tilde{x}$	$b_o + \tilde{y}$	$c_o + \tilde{z}$	1/2	--+	+	$a_o/4$	$-b_o/4$	0

TABLE I. Coordinates of the atoms in SmNiO_3 orthorhombic unit cell with lattice parameters $a_o = 5.328 \text{ \AA}$, $b_o = 5.437 \text{ \AA}$ and $c_o = 7.568 \text{ \AA}$ [13]. The numbers in brackets next to oxygen atoms indicate an index of Ni atom, relative to which the coordinates of the oxygen atoms are calculated (see **Equation S1** and **Figure S5b**). The coordinates $\tilde{\mathbf{u}} = (\tilde{x}, \tilde{y}, \tilde{z})$ for each oxygen atom are calculated according to **Equation S2**, in which the signs of rotation angles α , β and γ and the breathing distortion are specified in columns 7 and 8, and the values (x_0, y_0, z_0) for the undistorted lattice are specified in columns 9–11.

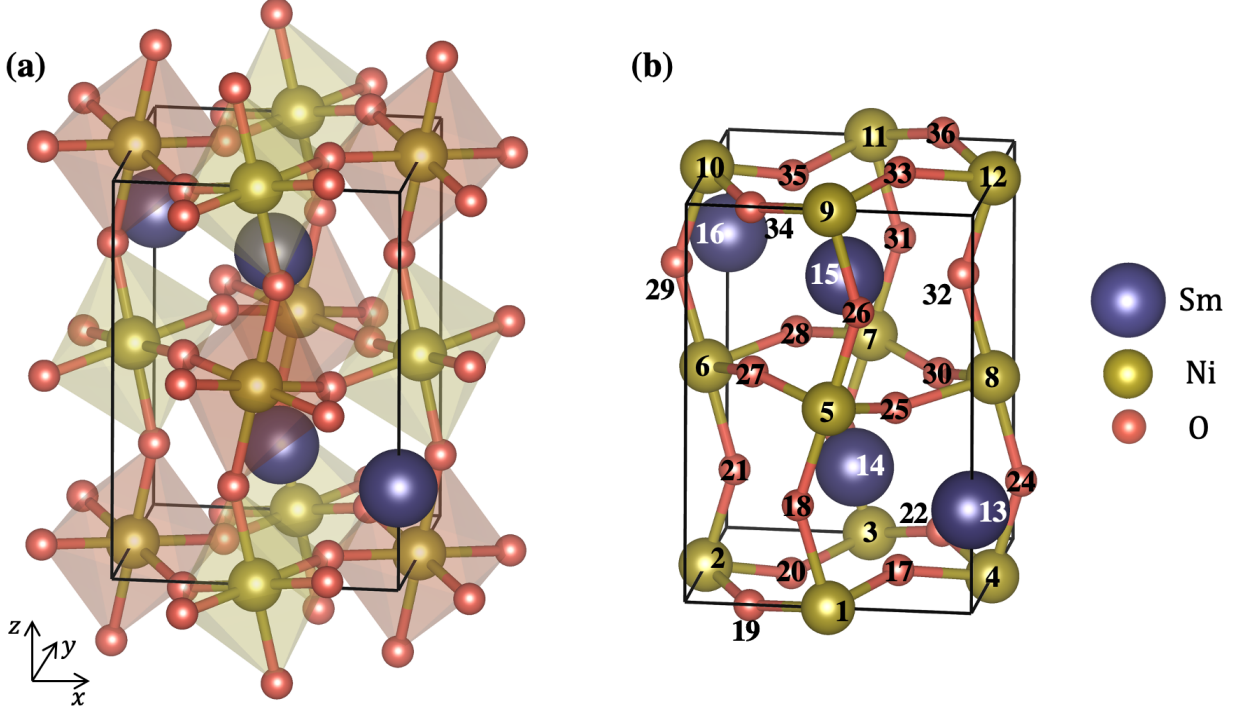


FIG. S5. (a) Orthorhombic unit cell of SmNiO₃ taken from the literature [13]. For better visualization, NiO₆ octahedra are shown around each Ni atom. The contracted octahedra are orange, and expanded are yellow (the breathing mode). (b) An identical unit cell of SmNiO₃ consisting of 36 atoms used for simulations of x-ray diffraction (see atomic coordinates in **Table I**). Only the atoms within a unit cell are shown. The numbers corresponds to the index j .

2. Rotation operator $\hat{R}(\alpha, \beta, \gamma)$

In this work, we assumed that the tilt of the NiO₆ octahedron can be described as a rotation of a rigid body. This allowed us to calculate the coordinates of each O atom by stretching the Ni–O bond (breathing mode) and rotating it relative to its position in the pristine SNO structure. It is known that rotations are not commutative, therefore the rotation operator $\hat{R}(\alpha, \beta, \gamma)$ can not be represented as three consecutive rotations around x -, y - and z -axis, because the final result will depend on the order of rotations. However for small angles, the rotation operators can be interchanged with the final result remaining constant up to the second-order terms [40]. Therefore, the rotation operator $\hat{R}(\alpha, \beta, \gamma)$ can be represented as a product of small commutative (Abelian) rotations around three orthogonal axes

$$\hat{R}(\alpha, \beta, \gamma) = \prod_{i=1}^N \hat{R}_x\left(\frac{\alpha}{N}\right) \hat{R}_y\left(\frac{\beta}{N}\right) \hat{R}_z\left(\frac{\gamma}{N}\right). \quad (\text{S3})$$

Here N is a large number (in our simulations we used $N = 100$), and $\hat{R}_x(\theta)$, $\hat{R}_y(\theta)$, and $\hat{R}_z(\theta)$ are operators of rotation about x -, y - and z -axis, respectively, with matrices

$$\hat{R}_x(\theta) = \begin{bmatrix} 1 & 0 & 0 \\ 0 & \cos \theta & -\sin \theta \\ 0 & \sin \theta & \cos \theta \end{bmatrix}, \quad (\text{S4})$$

$$\hat{R}_y(\theta) = \begin{bmatrix} \cos \theta & 0 & \sin \theta \\ 0 & 1 & 0 \\ -\sin \theta & 0 & \cos \theta \end{bmatrix}, \quad (\text{S5})$$

$$\hat{R}_z(\theta) = \begin{bmatrix} \cos \theta & -\sin \theta & 0 \\ \sin \theta & \cos \theta & 0 \\ 0 & 0 & 1 \end{bmatrix}. \quad (\text{S6})$$

We want to emphasize here that since we use the orthorhombic symmetry, all rotations in this work are performed about orthorhombic axes, and not about traditionally used pseudocubic axes [14].

3. Simulation of x-ray diffraction

The intensity of the diffracted beam I_{hkl} was calculated as the squared modulus of the form factor $F(\mathbf{q})$

$$I_{hkl} \propto |F(\mathbf{q})|^2, \quad (\text{S7})$$

where

$$F(\mathbf{q}) = \sum_{j=1}^{36} O_j f_j(q, E) \exp(i\mathbf{q}\mathbf{r}_j), \quad (\text{S8})$$

and index j runs over all atoms in the unit cell (see **Table I**). The atomic form factors $f_j(q, E)$ at x-ray energy $E = 8345$ eV were calculated for Sm^{3+} , Ni^{3+} and O^{2-} ions using Cromer-Mann parameterization [52] and tabulated energy-dependent corrections [53]. The components of the scattering vector $\mathbf{q} = (q_x, q_y, q_z)$ for the reflection (hkl) equal to $(2\pi h/a_o, 2\pi k/b_o, 2\pi l/c_o)$. In this work, we considered two groups of symmetry equivalent reflections: (101) and (202) – that corresponds to the $(\frac{1}{2}\frac{1}{2}\frac{1}{2})_{pc}$ and $(111)_{pc}$ reflections in pseudocubic notation, correspondingly. Due to orthorhombic twinning (the values of the lattice

parameters are close, but not exactly equal $a_o \approx b_o \approx c_o/\sqrt{2}$), it is impossible to distinguish between the individual reflections within each class, so the intensity of the (101) reflection was evaluated as the averaged value of (101), (10 $\bar{1}$), (011), and (01 $\bar{1}$) intensities [41]. In a similar way, the intensity of the (202) is actually averaged over (202), (20 $\bar{2}$), (022), and (02 $\bar{2}$) reflections.

Direct evaluation of the (101) and (202) peaks intensity showed that the first peak is approximately 250 times weaker and its intensity strongly depends on d_x component of the rare-earth cation displacement (see **Figure 4** in the main text). At the same time the intensity of the (202) reflection is not strongly affected by these distortions (i.e., the octahedral rotations, breathing mode and the displacement of rare-earth cations). Neglecting the weak contribution from Ni and O atoms in **Equation S8**, the form factors can be simplified to

$$F_{101,10\bar{1}} \propto \sin \frac{2\pi d_x}{a_o} \cos \frac{2\pi d_z}{c_o} , \quad (\text{S9})$$

$$F_{011,01\bar{1}} = 0 , \quad (\text{S10})$$

$$F_{202,20\bar{2}} \propto \cos \frac{4\pi d_x}{a_o} \cos \frac{4\pi d_z}{c_o} , \quad (\text{S11})$$

$$F_{022,02\bar{2}} \propto \cos \left(\frac{4\pi d_y}{b_o} \pm \frac{4\pi d_z}{c_o} \right) . \quad (\text{S12})$$

One can also study how the local defects influence the intensity of the x-ray reflection, i.e., what happens if the values of Sm³⁺ displacements d_x , d_y and d_z are not the same for all unit cells. The direct evaluation shows that if the displacements d_x , d_y and d_z follow a normal distribution with standard deviation σ_x , σ_y and σ_z , respectively, the intensity of the averaged (due to twinning) reflections can be estimated as

$$I_{101} \propto \exp \left[- \left(\frac{2\pi\sigma_x}{a_o} \right)^2 - \left(\frac{2\pi\sigma_z}{c_o} \right)^2 \right] \sin^2 \frac{2\pi d_x}{a_o} \cos^2 \frac{2\pi d_z}{c_o} , \quad (\text{S13})$$

$$\begin{aligned} I_{202} \propto & \exp \left[- \left(\frac{4\pi\sigma_x}{a_o} \right)^2 - \left(\frac{4\pi\sigma_z}{c_o} \right)^2 \right] \cos^2 \frac{4\pi d_x}{a_o} \cos^2 \frac{4\pi d_z}{c_o} + \\ & + \exp \left[- \left(\frac{4\pi\sigma_y}{b_o} \right)^2 - \left(\frac{4\pi\sigma_z}{c_o} \right)^2 \right] \cos^2 \left(\frac{4\pi d_y}{b_o} + \frac{4\pi d_z}{c_o} \right) + \\ & + \exp \left[- \left(\frac{4\pi\sigma_y}{b_o} \right)^2 - \left(\frac{4\pi\sigma_z}{c_o} \right)^2 \right] \cos^2 \left(\frac{4\pi d_y}{b_o} - \frac{4\pi d_z}{c_o} \right) . \end{aligned} \quad (\text{S14})$$

These results agree with the direct calculations with **Equations S7** and **S8**, shown in **Figure 4b,e** in the main text: the intensity of the (101) reflection can be estimated as $I_{101} \propto d_x^2$ for a small cation displacement. **Equations S13** and **S14** show how the experimentally measured intensities of Bragg reflections are related to the parameters of our structural model.

Supplemental Materials: DFT-simulations of SNO electronic structure

1. Magnetic considerations

SNO is known to be paramagnetic [14], however, the DFT calculations are limited to magnetically ordered (e.g., ferromagnetic or antiferromagnetic) or nonmagnetic systems. As such, one needs to select a proxy magnetic configuration based on structural consistency with experimental observations and stability of the doped H-SNO structure. We started by relaxing the orthorhombic phase of SNO shown in **Figure S5** under a nonmagnetic (NM), ferromagnetic (FM) and antiferromagnetic (AFM) configuration [43].

We used the Interstitialcy Finding Tool (InFiT) [54] to locate all possible interstitial sites for H under a 1H:32Ni ratio in SNO. We found that the formation energy of H-SNO in the FM phase was 70 meV more stable than in the T-AFM phase (**Figure S6**). In NM phase (zero-spin configuration), no band gap opening was observed with H-doping (see the next section), so this phase can not be used to study the doping effects. Hence all investigations of the effect of H-doping concentration on the oxidation state and x-ray absorption spectrum (XAS) were done in the FM phase.

2. Opening of the band gap with hydrogen doping

We tested the effect of H concentration on the density of states (DoS) in orthorhombic SNO (**Figure S7**). We observed that at concentrations below 1H:1Ni, orthorhombic SNO remains metallic, however at a 1H:1Ni ratio, a large band gap of 1.14 eV appears which is consistent with previous studies [31]. We observed that the integrated spin density of Ni in H-SNO gradually increases relative to the undoped system, which indicates that the Ni oxidation state increases with H concentration. The converged spin density of undoped SNO at 0.92 is associated with the Ni³⁺ cation. The integrated spin density associated with the

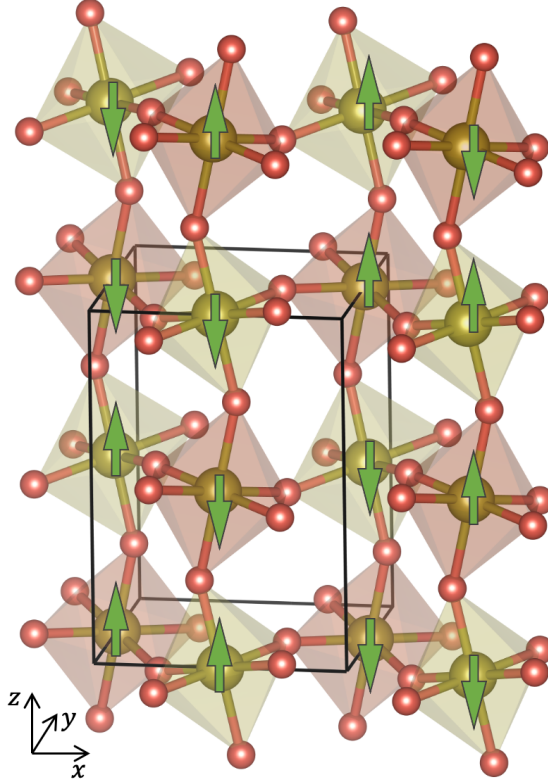


FIG. S6. Sketch of the spin configuration of the T-AFM phase characterized by the particular $\uparrow\uparrow\downarrow$ stacking along all three crystallographic directions [38]. The rare-earth cations are not shown for clarity, black lines represent the orthorhombic unit cell.

1H:1Ni concentration has a converged integrated spin density nearly doubled (1.7) that of the undoped SNO which is associated with the Ni^{2+} cation (**Figure S7b**). This supports the notion that a change in transition states is required for the opening of a band gap and thus formation of an insulating phase. In **Figure S7**, we considered several possible interstitial sites for each concentration and only showed the results for the most energetically stable configuration.

Next we evaluated the effect of valence change. We already calculated the DoS for a 1H:1Ni doped SNO structure under a non-zero spin configuration (**Figure S7i,j**) which results in a change of Ni valence from Ni^{3+} to Ni^{2+} . We also calculated the DoS of the same structure at a zero spin configuration (which corresponds to NM phase) which results in a change of Ni valence from Ni^{3+} to Ni^{4+} in **Figure S8a-b**. These calculations were done with the lattice and sites fixed at their relaxed undoped positions to isolate the valence effect from any structural distortion. Since we observed no band gap opening in NM phase (**Figure S8a**), this phase was excluded from further analysis. From **Figure S7** and

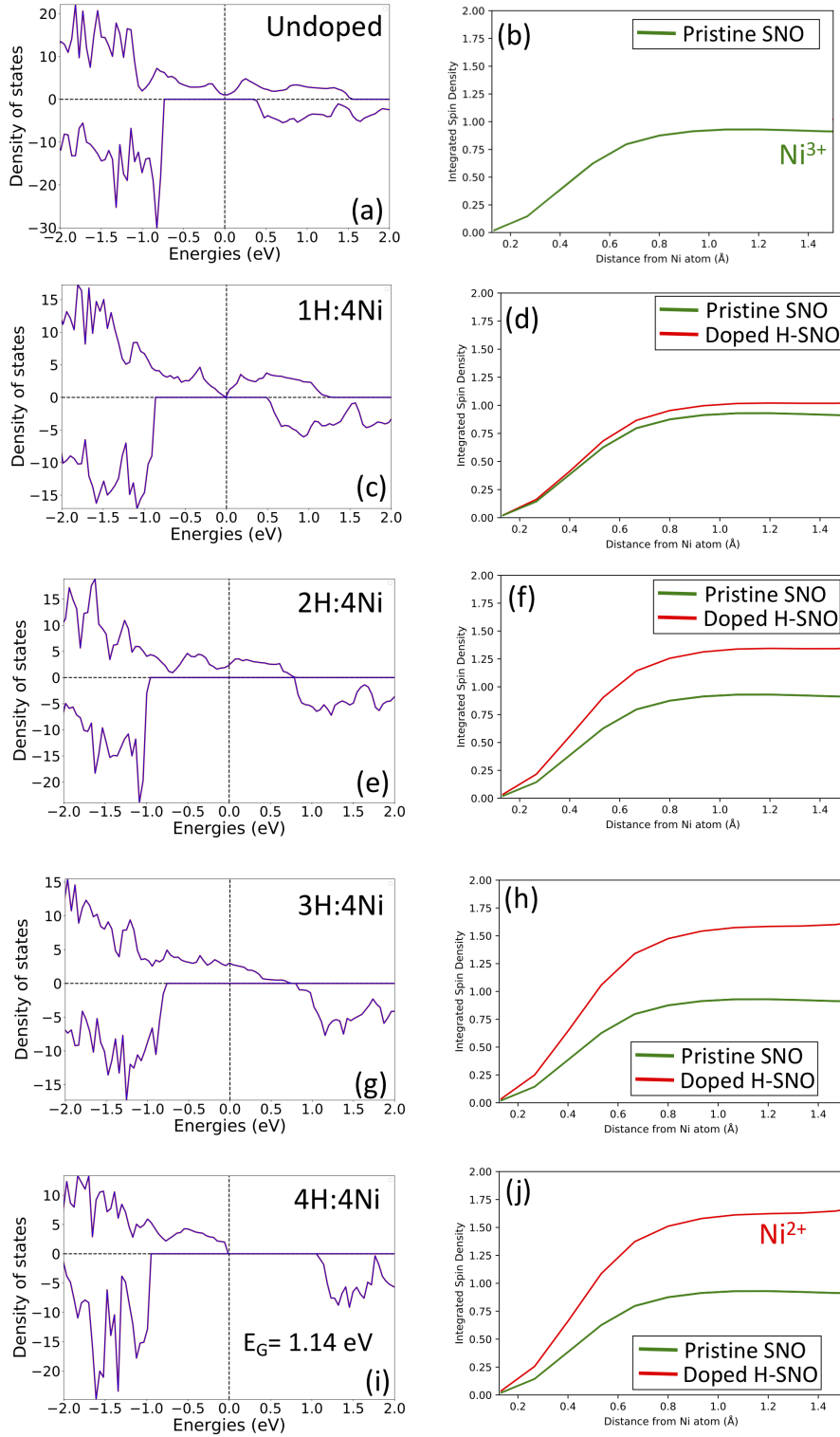


FIG. S7. The DoS (left column) and integrated spin density (right column) of H-doped orthorhombic SNO at various doping concentrations, namely no doping (a-b), 1H:4Ni (c-d), 1H:2Ni (e-f), 3H:4Ni (g-h), and 1H:1Ni (i-j). The integrated spin density of undoped orthorhombic SNO is shown in green as a reference for all doping levels.

Figure S8 we conclude, that the band gap opens only if the Ni valence decreases from 3+ (pristine SNO) to almost 2+ (1H:1Ni doping).

To decouple the structural and electronic effects of the H-doping on the band gap opening, we performed several calculations with some artificially introduced constrains. In **Figure S9a-b** the band gap opening is shown for 1H:1Ni doping when all atoms in the H-SNO structure are allowed to move in order to reach the most energetically stable configurations. This leads to the opening of the large band gap $E_G = 1.14$ eV, as we described earlier. However, if one only allows the Sm^{3+} ions (**Figure S9c,d**) or H^+ (**Figure S9e,f**) to relax, the band gap appears to be almost twice smaller. Contrary to that, if one only allows NiO_6 octahedra to relax (**Figure S9g,h**), the resulting band gap again becomes almost fully open. Specifically, the polyhedron volumes of NiO_6 increase from their undoped volume of 10.2 \AA^3 to 10.8 \AA^3 as a result of the decrease in the nickel oxidation state. This leads us to conclusion: the band gap opens in any case, when the level of H-doping is high enough, however, only combined effect of H-doping and structural changes in the NiO_6 octahedra can explain the final large value of $E_G \approx 1$ eV in the H-SNO. To assess the effect of pure structural distortion on the band gap opening, we performed the similar computations for the fully relaxed H-SNO structure without adding any H-dopants (**Figure S9i,j**). This structure shows no band gap, indicating that the prime contribution to the insulating properties of H-SNO comes from the electron doping and not from the structural changes.

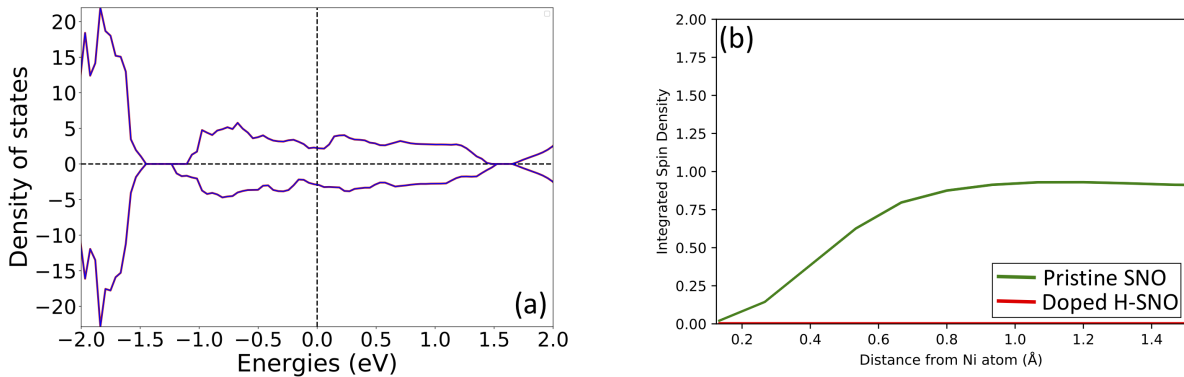


FIG. S8. The DoS (a) and integrated spin density (b) of H-doped orthorhombic SNO at zero-spin configuration (NM phase).

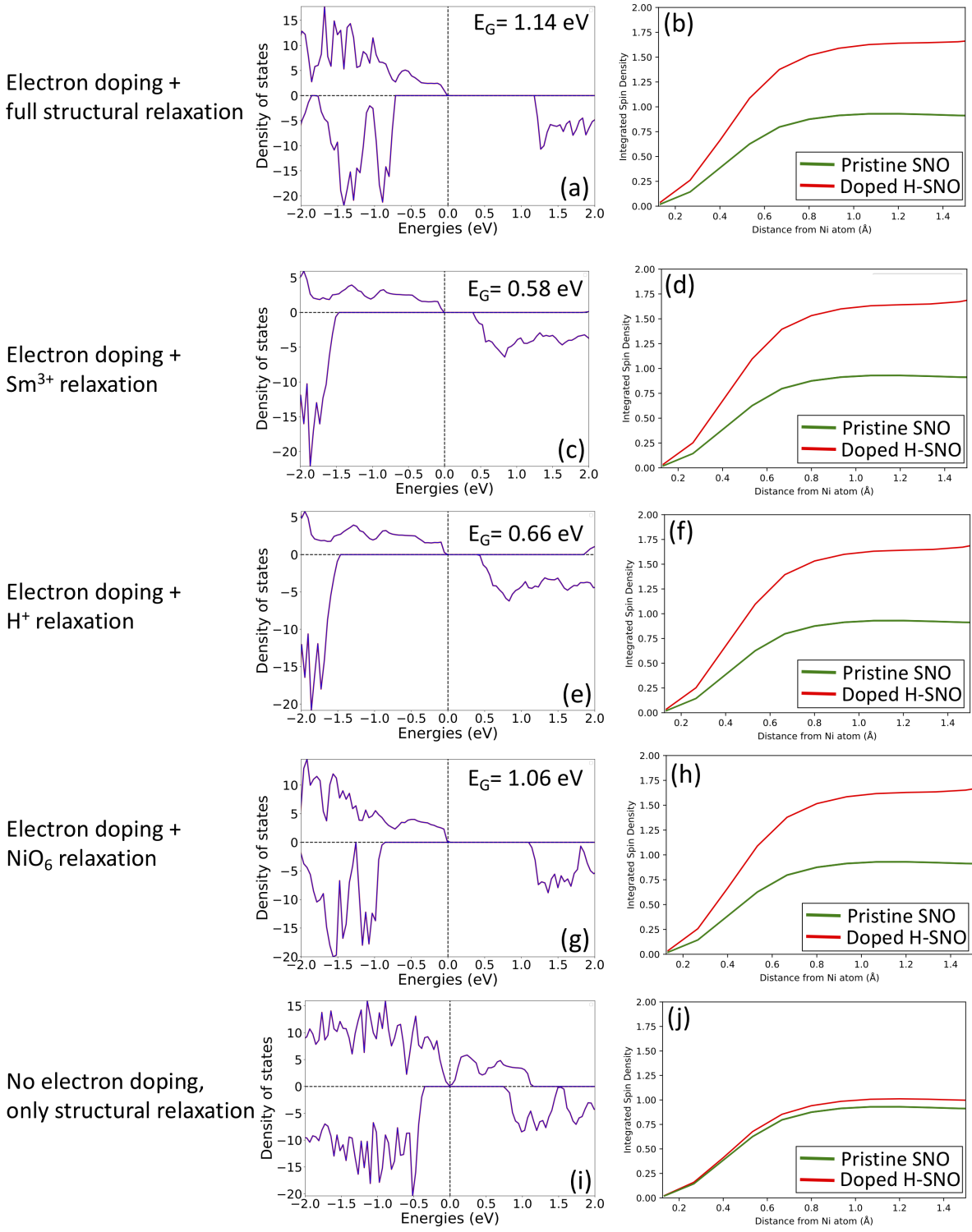


FIG. S9. The DoS (left column) and integrated spin density (right column) of H-doped orthorhombic SNO at 1H:1Ni concentration with full volume and H-site relaxation (a-b), with only Sm site relaxation (c-d), only H site relaxation (e-f), and only NiO_6 octahedra relaxation. Panels (i-j) show the results of the structural relaxation of H-SNO only, without electron doping from H-dopant.

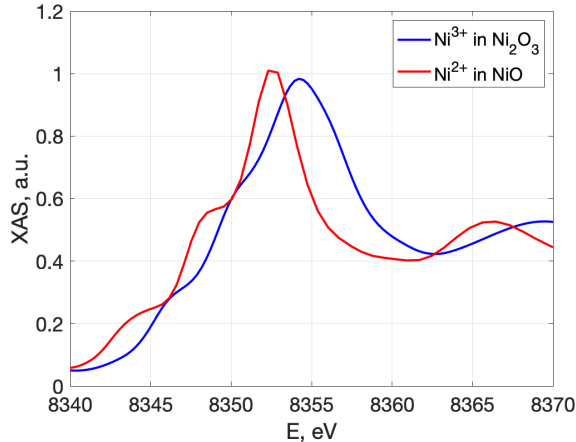


FIG. S10. FEFF-simulated normalized XAS spectra at the K-edge of Ni^{3+} in Ni_2O_3 (blue) and Ni^{2+} in NiO (red). The spectra were obtained from the Materials Project database [55, 56].

3. Comparison of XAS spectrum to known reference compounds

To directly explore the effect of Ni reduction in the XAS spectra, we presented the FEFF-simulated spectra for two reference compounds, NiO (Ni^{2+}) and Ni_2O_3 (Ni^{3+}). As shown in Figure S10, the K-edge of Ni in NiO oxide is approximately 1.75 eV lower than in Ni_2O_3 oxide. The same shift of approximately 1.2 eV was observed between the SNO and H-SNO in our experimental data, which suggests the reduction of nickel from Ni^{3+} in the pristine SNO to Ni^{2+} in the fully doped H-SNO. This shift can be interpreted as a cation losing its ability to attract electrons as the valence state decreases, thereby requiring less energy to excite electrons to emit X-rays.

4. Hydrogen doping in the monoclinic phase

SmNiO_3 can also exist in an insulating monoclinic phase ($P2_1/n$), which differs from the metallic orthorhombic phase ($Pbnm$) by a small Ni-O bond disproportionation in the form of a breathing-mode configuration (with a magnitude of $\sim 1 - 2\%$ in Ni-O bond length, which leads to the NiO_6 octahedra volume expansion/contraction of $\sim 10\%$). We performed DFT simulations to assess the effect of H-doping on the electronic properties of the monoclinic phase under a T-AFM spin configuration (**Figure S6**). The results are shown in **Figure S11a** where the band gap E_G is plotted as a function of the H-dopant concentration. The obtained value of the band gap $E_G \approx 0.2$ eV for the pristine monoclinic

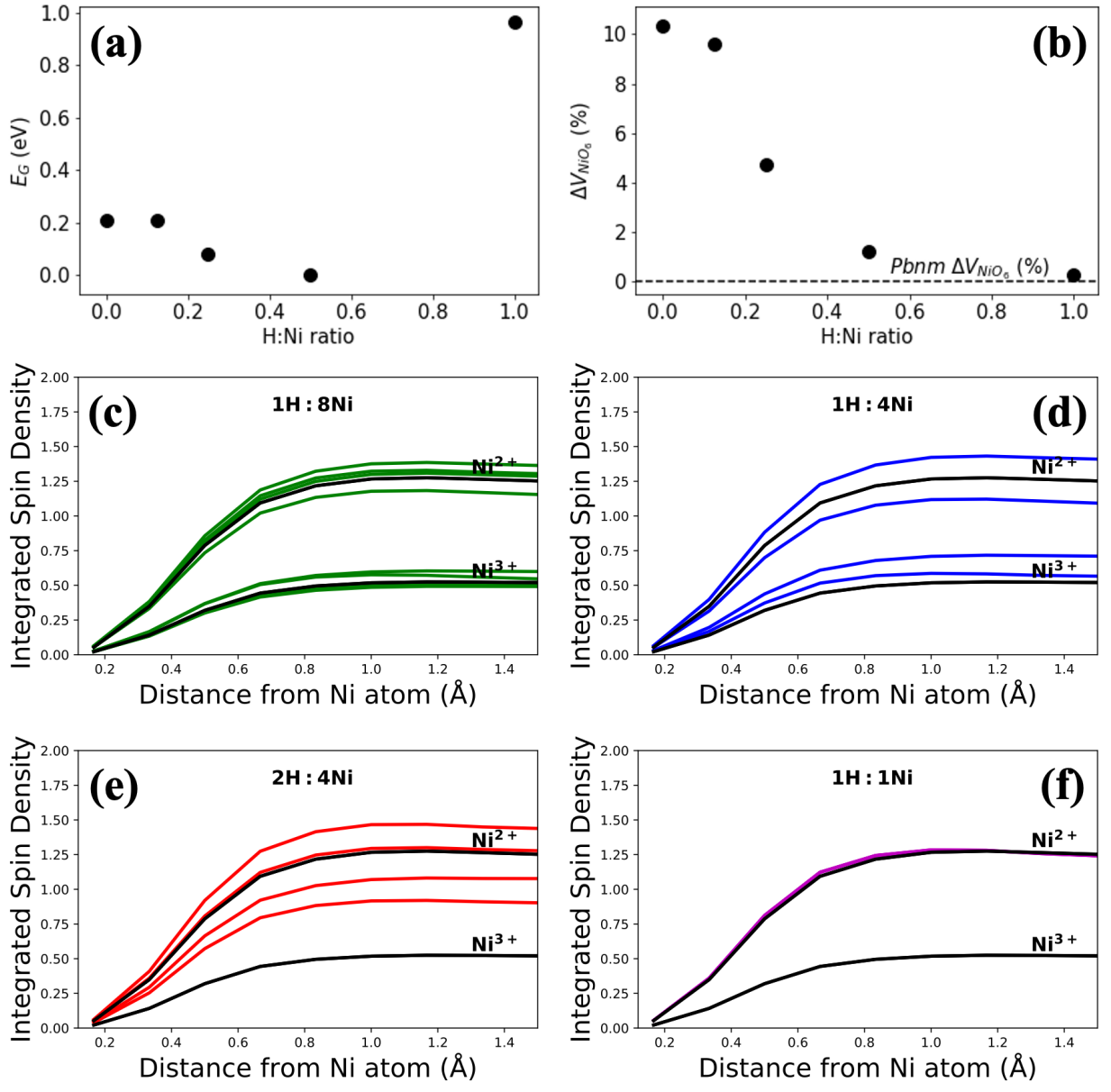


FIG. S11. The band gap E_G (a) and bond-disproportionation (b) of monoclinic insulating SmNiO₃ in the T-AFM phase is plotted against the H-doping level. Here, bond-disproportionation is defined as the percentage difference in volume of NiO₆ polyhedrons with opposite spins (see **Figure S6**). (c-f) The integrated spin density of H-doped monoclinic SNO at a ratio of 1H:8Ni (c), 1H:4Ni (d), 2H:4Ni (e) and 1H:1Ni (f). Color lines represent different nickel atoms in the doped H-SNO and black lines show the integrated spin density of the undoped SNO (all calculations are performed for the monoclinic phase).

SNO agrees with the published data [14], however as the H:Ni ratio increases, we observe a decrease in E_G until the gap disappears completely at a ratio of 1H:2Ni. This coincides with the gradual dissipation of breathing-mode (**Figure S11b**), as the difference in NiO₆ volumes

disappears, and the mixed valence states of $\text{Ni}^{2/3+}$ (shown in the black lines) converges to Ni^{2+} (**Figure S11c-e**). Increasing the ratio to 1H:1Ni in the monoclinic phase yields similar results to 1H:1Ni doping in the orthorhombic phase with all Ni-cations converging to a valence state of Ni^{2+} (**Figure S11f**) and the volume of all NiO_6 polyhedrons becoming uniform. Consequently, the band gap E_G in the monoclinic phase increases to the value of 0.97 eV, approximately five times the undoped band gap of the monoclinic phase. The absence of any noticeable band gap prior to the reduction of all nickel ions to the 2+ valence state is a further evidence that the decrease in electrical conductivity is connected to the valence state. This and the fact that our experimental data did not show any evidences of the significant bond disproportionation in both SNO and H-SNO justifies the focus on the orthorhombic phase in our DFT simulations.

-
- [1] S. Ramanathan, MRS Bull. **43**, 534 (2018).
 - [2] K. Roy, A. Jaiswal, and P. Panda, Nature **575**, 607 (2019).
 - [3] H.-T. Zhang, P. Panda, J. Lin, Y. Kalcheim, K. Wang, J. W. Freeland, D. D. Fong, S. Priya, I. K. Schuller, S. K. R. S. Sankaranarayanan, K. Roy, and S. Ramanathan, Appl. Phys. Rev. **7**, 11309 (2020).
 - [4] J. del Valle, J. G. Ramírez, M. J. Rozenberg, and I. K. Schuller, J. Appl. Phys. **124**, 211101 (2018).
 - [5] H.-T. Zhang, T. J. Park, I. A. Zaluzhnyy, Q. Wang, S. N. Wadekar, S. Manna, R. Andrawis, P. O. Sprau, Y. Sun, Z. Zhang, C. Huang, H. Zhou, Z. Zhang, B. Narayanan, G. Srinivasan, N. Hua, E. Nazaretski, X. Huang, H. Yan, M. Ge, Y. S. Chu, M. J. Cherukara, M. V. Holt, M. Krishnamurthy, O. G. Shpyrko, S. K. Sankaranarayanan, A. Frano, K. Roy, and S. Ramanathan, Nat. Commun. **11**, 2245 (2020).
 - [6] J. Shi, S. D. Ha, Y. Zhou, F. Schoofs, and S. Ramanathan, Nat. Commun. **4**, 2676 (2013).
 - [7] J. Zhu, T. Zhang, Y. Yang, and R. Huang, Appl. Phys. Rev. **7**, 011312 (2020).
 - [8] K. Ramadoss, F. Zuo, Y. Sun, Z. Zhang, J. Lin, U. Bhaskar, S. Shin, M. A. Alam, S. Guha, D. Weinstein, and S. Ramanathan, IEEE Electron Device Lett. **39**, 1500 (2018).
 - [9] U. Staub, G. I. Meijer, F. Fauth, R. Allenspach, J. G. Bednorz, J. Karpinski, S. M. Kazakov, L. Paolasini, and F. d'Acapito, Phys. Rev. Lett. **88**, 126402 (2002).

- [10] Y. Lu, A. Frano, M. Bluschke, M. Hepting, S. Macke, J. Stremper, P. Wochner, G. Cristiani, G. Logvenov, H.-U. Habermeier, M. W. Haverkort, B. Keimer, and E. Benckiser, *Phys. Rev. B* **93**, 165121 (2016).
- [11] J. Chen, W. Mao, B. Ge, J. Wang, X. Ke, V. Wang, Y. Wang, M. Döbeli, W. Geng, H. Matsuzaki, J. Shi, and Y. Jiang, *Nat. Commun.* **10**, 694 (2019).
- [12] A. M. Glazer, *Acta Cryst. B* **28**, 3384 (1972).
- [13] A. Jain, S. P. Ong, G. Hautier, W. Chen, W. D. Richards, S. Dacek, S. Cholia, D. Gunter, D. Skinner, G. Ceder, and K. A. Persson, *APL Mater.* **1**, 11002 (2013).
- [14] S. Catalano, M. Gibert, J. Fowlie, J. Íñiguez, J.-M. Triscone, and J. Kreisel, *Rep. Prog. Phys.* **81**, 46501 (2018).
- [15] A. M. Glazer, *Acta Cryst. A* **31**, 756 (1975).
- [16] J. Shi, Y. Zhou, and S. Ramanathan, *Nat. Commun.* **5**, 4860 (2014).
- [17] Y. Zhou, X. Guan, H. Zhou, K. Ramadoss, S. Adam, H. Liu, S. Lee, J. Shi, M. Tsuchiya, D. D. Fong, and S. Ramanathan, *Nature* **534**, 231 (2016).
- [18] K. Ramadoss, N. Mandal, X. Dai, Z. Wan, Y. Zhou, L. Rokhinson, Y. P. Chen, J. Hu, and S. Ramanathan, *Phys. Rev. B* **94**, 235124 (2016).
- [19] Y. Sun, M. Kotiuga, D. Lim, B. Narayanan, M. Cherukara, Z. Zhang, Y. Dong, R. Kou, C.-J. Sun, Q. Lu, I. Waluyo, A. Hunt, H. Tanaka, A. N. Hattori, S. Gamage, Y. Abate, V. G. Pol, H. Zhou, S. K. R. S. Sankaranarayanan, B. Yildiz, K. M. Rabe, and S. Ramanathan, *Proc. Natl. Acad. Sci. U.S.A.* **115**, 9672 (2018).
- [20] Z. Liao, N. Gauquelin, R. J. Green, K. Müller-Caspary, I. Lobato, L. Li, S. Van Aert, J. Verbeeck, M. Huijben, M. N. Grisolia, V. Rouco, R. El Hage, J. E. Villegas, A. Mercy, M. Bibes, P. Ghosez, G. A. Sawatzky, G. Rijnders, and G. Koster, *Proc. Natl. Acad. Sci. U.S.A.* **115**, 9515 (2018).
- [21] See Supplemental Material for supporting details on experiment, simulations of x-ray diffraction, and DFT calculations.
- [22] A. Mansour N. and C. Melendres A., *J. Phys. IV France* **7**, 1171 (1997).
- [23] R. J. Woolley, B. N. Illy, M. P. Ryan, and S. J. Skinner, *J. Mater. Chem.* **21**, 18592 (2011).
- [24] W. Gu, H. Wang, and K. Wang, *Dalton Trans.* **43**, 6406 (2014).
- [25] F. Zuo, P. Panda, M. Kotiuga, J. Li, M. Kang, C. Mazzoli, H. Zhou, A. Barbour, S. Wilkins, B. Narayanan, M. Cherukara, Z. Zhang, S. K. R. S. Sankaranarayanan, R. Comin, K. M. Rabe,

- K. Roy, and S. Ramanathan, *Nat. Commun.* **8**, 240 (2017).
- [26] Z. Zhang, D. Schwanz, B. Narayanan, M. Kotiuga, J. A. Dura, M. Cherukara, H. Zhou, J. W. Freeland, J. Li, R. Sutarto, F. He, C. Wu, J. Zhu, Y. Sun, K. Ramadoss, S. S. Nonnenmann, N. Yu, R. Comin, K. M. Rabe, S. K. R. S. Sankaranarayanan, and S. Ramanathan, *Nature* **553**, 68 (2018).
- [27] M. Kotiuga and K. M. Rabe, *Phys. Rev. Mater.* **3**, 115002 (2019), 1909.03425.
- [28] G. Kresse and J. Furthmüller, *Phys. Rev. B* **54**, 11169 (1996).
- [29] G. Kresse and D. Joubert, *Phys. Rev. B* **59**, 1758 (1999).
- [30] J. J. Rehr, J. J. Kas, F. D. Vila, M. P. Prange, and K. Jorissen, *Phys. Chem. Chem. Phys.* **12**, 5503 (2010).
- [31] P. Yoo and P. Liao, *Mol. Syst. Des. Eng.* **3**, 264 (2018).
- [32] P. Yoo and P. Liao, *Phys. Chem. Chem. Phys.* **22**, 6888 (2020).
- [33] U. Goteti, I. A. Zaluzhnyy, S. Ramanathan, R. C. Dynes, and A. Frano, *Proc. Natl. Acad. Sci. U.S.A.* (2021), 10.1073/pnas.2103934118.
- [34] J. A. Alonso, J. L. García-Muñoz, M. T. Fernández-Díaz, M. A. G. Aranda, M. J. Martínez-Lope, and M. T. Casais, *Phys. Rev. Lett.* **82**, 3871 (1999).
- [35] R. J. Green, M. W. Haverkort, and G. A. Sawatzky, *Phys. Rev. B* **94**, 195127 (2016).
- [36] F. Serrano-Sánchez, F. Fauth, J. L. Martínez, and J. A. Alonso, *Inorg. Chem.* **58**, 11828 (2019).
- [37] N. A. Benedek and C. J. Fennie, *J. Phys. Chem. C* **117**, 13339 (2013).
- [38] J. Varignon, M. N. Grisolia, J. Íñiguez, A. Barthélémy, and M. Bibes, *npj Quantum Mater.* **2**, 21 (2017).
- [39] Historically these rotations were introduced for the pseudocubic symmetry. The same tilt of the NiO₆ octahedra can be obtained by rotation over 10.8°, 10.8°, and 7.0° around the [100]_{pc}, [010]_{pc}, and [001]_{pc} pseudocubic directions, respectively.
- [40] J. Fowlie, C. Lichtensteiger, M. Gibert, H. Meley, P. Willmott, and J.-M. Triscone, *Nano Lett.* **19**, 4188 (2019).
- [41] M. Brahlek, A. K. Choquette, C. R. Smith, R. Engel-Herbert, and S. J. May, *J. Appl. Phys.* **121**, 45303 (2017).
- [42] M. Hepting, *Ordering Phenomena in Rare-Earth Nickelate Heterostructures*, Springer Theses (Springer International Publishing, Cham, 2017).

- [43] H. Yan, N. Bouet, J. Zhou, X. Huang, E. Nazaretski, W. Xu, A. P. Cocco, W. K. S. Chiu, K. S. Brinkman, and Y. S. Chu, *Nano Futures* **2**, 011001 (2018).
- [44] E. Nazaretski, H. Yan, K. Lauer, N. Bouet, X. Huang, W. Xu, J. Zhou, D. Shu, Y. Hwu, and Y. S. Chu, *J. Synchrotron Radiat.* **24**, 1113 (2017).
- [45] A. Pattammattel, R. Tappero, M. Ge, Y. S. Chu, X. Huang, Y. Gao, and H. Yan, *Sci. Adv.* **6**, eabb3615 (2020).
- [46] G. Kresse and J. Furthmüller, *Phys. Rev. B* **54**, 11169 (1996).
- [47] W. Kohn and L. J. Sham, *Phys. Rev.* **140**, 1133 (1965).
- [48] P. E. Blöchl, *Phys. Rev. B* **50**, 17953 (1994).
- [49] J. P. Perdew, K. Burke, and M. Ernzerhof, *Phys. Rev. Lett.* **77**, 3865 (1996).
- [50] V. I. Anisimov, J. Zaanen, and O. K. Andersen, *Phys. Rev. B* **44**, 943 (1991).
- [51] S. P. Ong, W. D. Richards, A. Jain, G. Hautier, M. Kocher, S. Cholia, D. Gunter, V. L. Chevrier, K. A. Persson, and G. Ceder, *Comput. Mater. Sci.* **68**, 314 (2013).
- [52] P. Brown, A. G. Fox, E. N. Maslen, M. A. O’Keefe, and B. T. M. Willis, *International Tables for Crystallography (Vol. C)* (2006) pp. 554–595.
- [53] C. T. Chantler, *J. Phys. Chem. Ref. Data* **24**, 71 (1995).
- [54] N. E. Zimmermann, M. K. Horton, A. Jain, and M. Haranczyk, *Front. Mater.* **4**, 34 (2017).
- [55] S. P. Ong, S. Cholia, A. Jain, M. Brafman, D. Gunter, G. Ceder, and K. A. Persson, *Comput. Mater. Sci.* **97**, 209 (2015).
- [56] C. Zheng, K. Mathew, C. Chen, Y. Chen, H. Tang, A. Dozier, J. J. Kas, F. D. Vila, J. J. Rehr, L. F. Piper, K. A. Persson, and S. P. Ong, *Npj Comput. Mater.* **4**, 1 (2018).